Journal of Sustainable Development of Energy, Water and Environment Systems

http://www.sdewes.org/jsdewes

Year 2026, Volume 14, Issue 3, 1140718

Original Research Article

Modeling, Optimization and Economic Analysis of Linear Fresnel Reflector for Direct Steam Generation for Tea Factories in Kenya

Edwin Moikoyo[1], Francis Njoka[1*], Evan M. Wanjiru[2]

[1]Department of Energy, Gas & Petroleum Engineering, Kenyatta University, P.O. Box 43844-00100, Nairobi, Kenya.

[2]Department of Mechatronic Engineering, Jomo Kenyatta University of Agriculture and Technology, P.O. Box 62000-00200, Nairobi, Kenya.

e-mail: njoka.francis@.ku.ac.ke

Cite as: Moikoyo, E., Njoka, F., Wanjiru, E. M., Modeling, Optimization and Economic Analysis of Linear Fresnel Reflector for Direct Steam Generation for Tea Factories in Kenya, J.sustain. dev. energy water environ. syst., 14(3), 1140718, 2026, DOI: https://doi.org/10.13044/j.sdewes.d14.0718

ABSTRACT

The Linear Fresnel reflector is a promising solar concentrating technology for industrial process heat applications. This study optimizes key solar field geometric parameters to maximize optical efficiency and determines optimal system size based on solar multiple and tea factory thermal energy demand. The optimized solar field is integrated into a dynamic simulation model that analyzes hourly performance, incorporating steam storage and fuelwood hybridization for continuous supply. Economic performance is evaluated using simple payback period, levelized cost of heat, net present value and internal rate of return. The optimal configuration – receiver height of 4.4 m, mirror width of 0.5 m, mirror row spacing of 0.2 m – achieves a maximum 66.28% optical efficiency. A solar multiple of 2.25 provides 14 hours of storage, yielding average solar fractions of 0.5915 and 0.3853 during high and low irradiance months, respectively. The hybrid system reduces annual woodlot consumption and carbon dioxide emissions by 48.84%.

KEYWORDS

Linear Fresnel reflector, Tonatiuh, MATLAB, Thermal efficiency, Levelized cost of heat.

INTRODUCTION

The global industrial energy demand currently accounts for about 29% of the total final energy consumption [1]. Fossil fuels dominate this sector's energy supply. Their continued use has intensified climate change, contributing a substantial share of global greenhouse gas emissions [2]. Integrating renewables into the industrial energy mix can significantly reduce emissions, with a 1% increase in renewable energy adoption leading to a 0.98% decrease in emissions [3]. The approach could reduce emissions by up to 1.5 Gigatons annually, achieving net-zero emissions by 2050 [4], [5]. This transition is essential for achieving global climate targets and reducing the sector's carbon footprint.

Solar energy emerges as a promising renewable energy resource for industrial heat applications due to its widespread availability and zero direct emissions [6]. Among line-focus Concentrated Solar Power (CSP) technologies, the linear Fresnel reflector (LFR) is characterized by simpler design, low installation and maintenance costs and low land use

* Corresponding author

compared to parabolic trough collectors (PTC), which employ continuously curved mirrors. While PTCs generally achieve higher optical efficiencies due to shorter optical paths and stronger concentration ratios, they are associated with comparatively higher capital intensity and mechanical complexity. In contrast, non-concentrating technologies such as evacuated tube collectors offer lower upfront investment costs and operational simplicity but generally require larger collector areas to satisfy industrial-scale thermal demand [7], [8]. The LFR technology therefore provides a balanced trade-off between technical performance, land utilization and cost implications, making it a competitive alternative for large scale solar process heat integration.

An LFR system comprises of a reflector field and a fixed receiver. The reflector comprises an array of flat or slightly curved mirrors that focus direct solar radiation onto one or more stationary absorber tubes positioned above the mirror field. These tubes carry a heat transfer fluid (HTF), which is heated to temperatures up to 400 °C. The system has a geometric concentration ratio of 10-50. To enhance optical performance, an additional reflector positioned above the absorber tube redirects otherwise spilled radiation back onto the tube surface [9], [10].

Due to the relatively low outlet temperature of the solar field compared to point-focusing technologies, LFR is especially well-suited for direct steam generation (DSG) [11]. Their modular design enables easy scaling to meet varying heat demands across different applications [12]. DSG systems have a steam drum which separates the two- phase flow, delivering saturated steam to the network. Moreover, LFR DSG systems can be integrated with steam accumulators for thermal energy storage, and be hybridized with other sources, ensuring continuous heat supply for uninterrupted industrial operations [13]. These factors underline the growing recognition of LFR in the transition towards sustainable industrial energy solutions.

As an industrial process, tea processing is energy-intensive, consuming between 3.5 kWh and 10 kWh of thermal energy per kilogram of made tea (kg MT) [14], [15]. In Kenya, fuelwood serves as the primary energy source, emitting 2.27 kg carbon dioxide (CO_2) per kg MT [16], [17]. The tea industry's heavy reliance on fuelwood also accelerates deforestation. On average, a single tea factory consumes 11,500 trees annually to produce 3,450,000 kg MT, resulting in approximately 7,831 metric tons of CO_2 emissions [18]. To address these challenges and enhance the sustainability of Kenya's tea industry, there is a need to adopt the use of LFR for process heat requirements.

Over recent decades, researchers have endeavoured to improve the LFR system's performance by employing both simulations and experimental methods to analyze their optical, thermal and economic performance. A predominant area of focus in optimization research has been the solar field parameters. Nixon & Davies [19] optimized solar field's mirror row spacing, recommending uneven row spacing to induce shadowing at a transversal angle of 45°, thereby improving system performance. Similarly, Song *et al.* [20] developed a mathematical model to compute optical losses in LFR solar fields, concluding that the optimal receiver height should exceed 3 m. Babu *et al.* [21] optimized LFR systems with horizontal absorber and varying primary collector widths. Optimal configuration comprised of 29 reflectors with widths varying between 0.03 m and 0.06 m and a focal length of 0.96 m. Pulido-Iparraguirre *et al.* [12] presented optimized optical design by modifying three parameters of a standard collector, comparing it with a conventional design. Their results showed that modifications in concentrator displacement, receiver tilt and East-West concentrator rotation resulted in a monthly energy collection increase of 2% to 61%. Barbon *et al.* [22] proposed a mathematical model for optimization of the length of primary mirrors, mirror spacing and mirror width in small-scale LFRs. Despite these contributions, most optical optimizations have been restricted to a limited subset of solar-field variables, with other coupled parameters that influence optical performance generally assumed constant.

Integrated studies that combine technical and economic analyses remain scarse. Baba *et al.* [23] assessed the cost-effectiveness of LFR systems through optical, thermal and storage modeling. Their study compared scenarios involving existing boilers and LFR systems. Their payback periods for replacing the boilers with LFR systems ranged from 2 to 6 years. Moghimi *et al.* [24] optimized the solar field parameters, insulation of a multi-tube cavity receiver while determining the levelized cost of electricity of the LFR plant. However, these studies relied on payback period and levelized cost metrics without extending the analysis to additional profitability indicators such as internal rate of return (*IRR*) and net present value (*NPV*), which are essential for assessing financial feasibility.

A review of existing literature indicates that optical optimization of LFR systems has largely focused on a limited number of solar field variables, with interacting geometrical parameters commonly treated independently or held constant. Furthermore, most optimization studies assess collector performance in isolation, without linking geometric design to dynamic system operation under real industrial load profiles. Industrial applications such as tea production – characterized by continuous steam demand and seasonal variability – are rarely incorporated into LFR design frameworks. From an economic standpoint, prior studies frequently rely on single profitability indicators, limiting assessment of long-term financial sustainability.

The present study addresses these limitations through an integrated and application driven framework tailored to direct steam generation in Kenyan tea factories. First, an optical-thermal model is developed to evaluate useful heat gain and losses of the working fluid, tracking its thermodynamic state from subcooled liquid to saturation. Three key solar field geometric parameters – mirror width, row spacing and receiver height – are then simultaneously optimized using a mathematically formulated objective function implemented in MATLAB to maximize optical efficiency by minimizing shading, blocking and spillage losses. The optimized solar field is subsequently integrated within a dynamic model that simulates hourly system performance, incorporating steam storage and fuelwood hybridization to ensure reliable energy dispatch under variable solar conditions. Finally, the technical assessment is complemented by a comprehensive multi-metric economic evaluation incorporating simple payback period, levelized cost of heat, net present value and internal rate of return, with a sensitivity analysis covering performance uncertainties, capital and operating cost variability and macroeconomic fluctuations.

By integrating multi-parameter geometric optimization, dynamic hybrid system performance modeling, and comprehensive economic assessment within a site-specific industrial context, this study advances LFR research from component level optimization towards holistic system-level development analysis.

MATERIALS AND METHODS

This section outlines the study area, the development and validation of the optical and thermal models, optimization of the solar field and system size, performance and economic analysis of the LFR system.

Characteristics of the Study Site

The study was conducted at Momul Tea Factory, located at latitude 0.4° South and longitude 35.1° East, approximately 269 km Northwest of Nairobi city. Situated in the country's largest tea producing regions, the factory presents a significant opportunity for renewable energy integration. The study focused on four critical data categories: solar resource availability, climatic conditions, thermal energy demands and cost of tea production. Data on solar resource availability and climatic conditions were obtained from Akello *et al.* [25] and Kenya Meteorological Department (KMD), respectively. The steam properties data, thermal energy demand and costs were directly collected from the factory.

Model Development

Mathematical modeling. Mathematical modeling of LFR was conducted to compute the useful energy harnessed from solar radiation by the thermal fluid at the factory location. The modeling framework comprised two main components: optical and thermal models. The optical model evaluated the optical efficiency of the collector, which is influenced by the sun's position, geometry of the collector, reflectivity of its components and incidence angle modifier. The critical solar angles that influence the redirection of reflected solar radiation towards the receiver were determined. **Figure 1** illustrates these critical angles, including the longitudinal angle of incidence, Φ_L, and transversal incidence angle, Φ_T, along with their determinants. A north-south (N-S) mirror orientation was chosen for this study since it optimizes annual irradiance utilization, particularly at solar noon [26], [27].

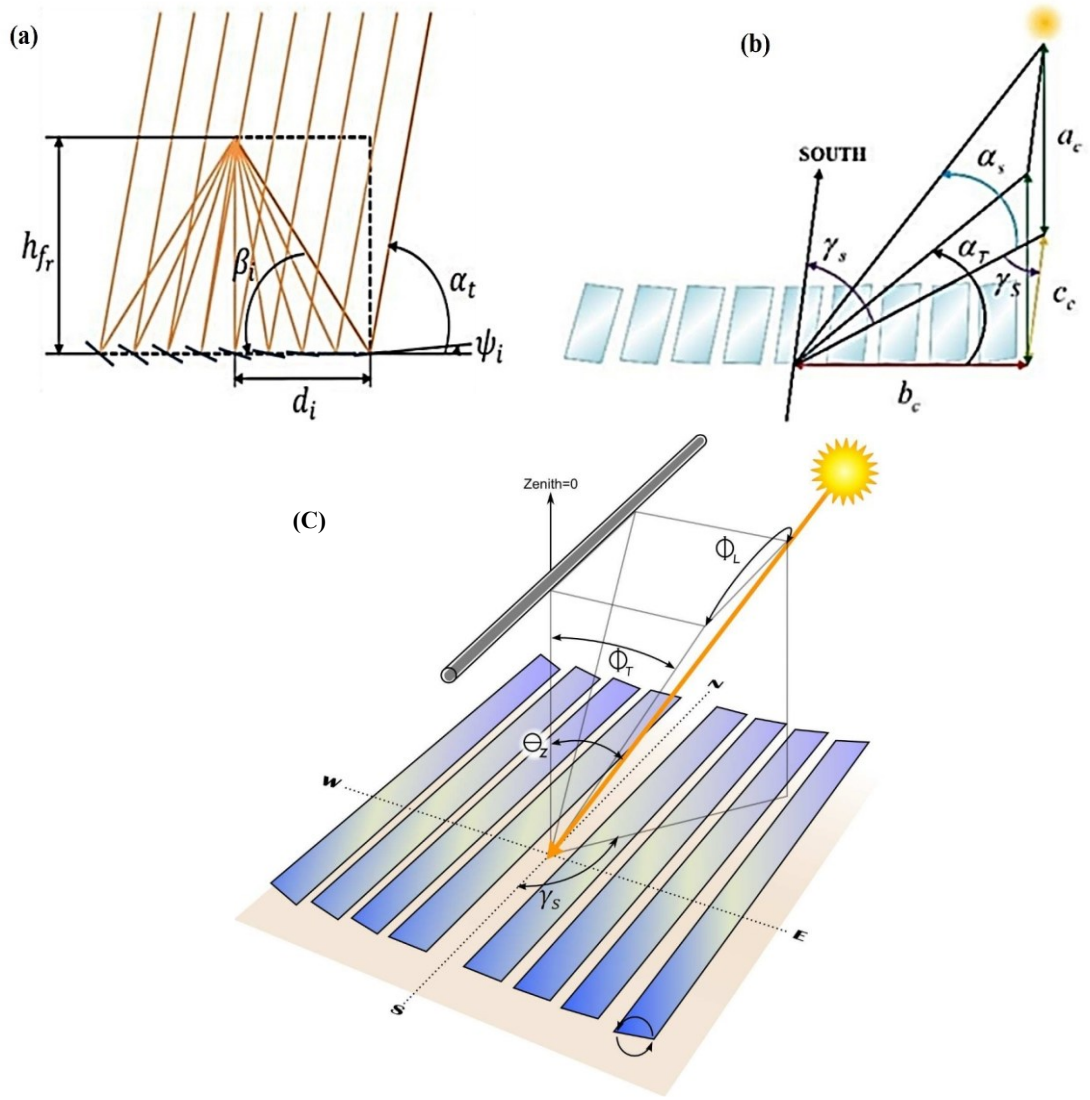

Figure 1. LFR system angles (a) Mirror inclination angle and (b) Transverse solar altitude angle and (c) Longitudinal and transversal incidence angles [27], [28]

The mirror inclination angle, ψ_i was calculated using eq. (1) [27]:

$$\psi_i = \frac{\alpha_T - \beta_i}{2} \quad (1)$$

To determine the angle between reflecting surface of the ith mirror and horizontal ground plane, β_i, the dependence on the receiver height above the primary mirrors, h_{fr}, and the transversal location of the ith mirror, d_i, were considered, as shown in eq. (2):

$$\beta_i = \arctan\left(\frac{h_{fr}}{d_i}\right) \tag{2}$$

Correlations for the other critical parameters were adopted from reference models as detailed in **Table 1**.

Table 1. Optical model parameters

Parameter	**Reference model**
Transverse solar altitude angle (α_T)	[27]
Solar altitude angle (α_s)	[29]
Local solar time	[30]
Solar azimuth angle (γ_s)	[27]
Incident angle modifier (IAM) (K (Φ_L, Φ_T))	[28], [31], [32], [33]

The other two key parameters for computing optical efficiency: the incident power on the collector's surface directly from the sun (P_{Ap}) and the incident power on the absorber tube, after reflection by primary mirrors (P_{abs}) are given by eq. (3) and eq. (4) [34]:

$$P_{Ap} = DNI \times A_p \times \cos(\theta_z) \tag{3}$$

where DNI represents location's direct normal irradiance (W/m^2) and A_p denotes area of collector's aperture (m^2) and θ_z is the Zenith angle.

$$P_{abs} = N_{Ph} \times P_{Ph} \tag{4}$$

where N_{ph} represents the number of photons reaching the absorber's surface, and P_{ph} denotes individual photon's power (W) at a specific location. P_{ph} was determined using Tonatiuh software, a Monte Carlo Ray Tracing (MCRT) tool [35].

The geometry-dependent determinants of the number of photons reaching the absorber's surface, N_{ph}, namely, intercept, shading loss and blocking loss factors were then determined. Appendix A1 provides correlations for computing these determinants. To account for additional optical losses from mirror surface imperfections, the nominal mirror reflectivity of the reference collector was reduced from 0.95 to 0.88 in the Tonatiuh simulations, consistent with reported reductions due to soiling [36].

The collector's optical efficiency was then calculated using eq. (5):

$$\eta_{opt} = \frac{P_{abs}}{P_{Ap}} \tag{5}$$

The thermal model, on the other hand, was developed to calculate the energy absorbed by the heat transfer fluid and thermal efficiency while accounting for heat losses from the receiver to the atmosphere. Here, a one-dimensional heat transfer model of an evacuated tube receiver with secondary reflector was developed. This approach was chosen because one-dimensional

models, when developed with sufficient physical detail have demonstrated a good agreement with experimental data [36]. Appendix A2 illustrates the heat flow in the receiver and outlines the correlations for heat transfer.

A thermal energy balance algorithm was developed in MATLAB to evaluate the heat gain and losses per unit length along the absorber tube. The model couples local energy balance with temperature-dependent thermophysical properties of water and steam obtained directly from the XSteam library, allowing continuous tracking of the fluid's thermodynamic state from sub-cooled liquid at the inlet temperature, T_i, of 87 °C to saturated conditions at the outlet temperature, T_o, of 188.15 °C and a pressure of 12 bar.

The algorithm progresses axially along the receiver in uniform segments of 0.5 m. At each segment, N, the inlet and outlet heat transfer fluid temperatures, $(T_{HTF,i})_N$ and $(T_{HTF,o})_N$ are determined, computing absorbed solar energy, convective heat transfer to the working fluid and the external convective and radiative losses. The sections are shown in **Figure 2**.

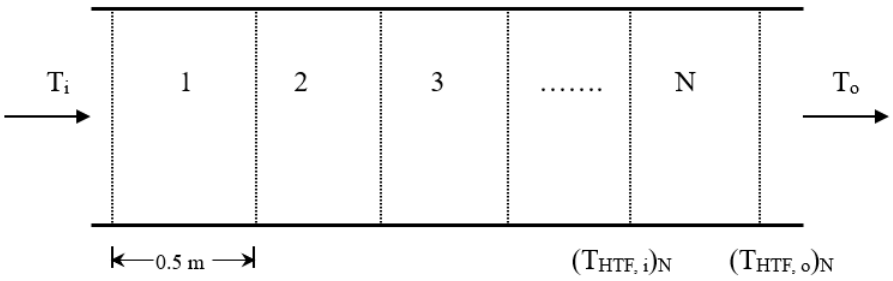

Figure 2. Axial portioning of absorber tube

The convective heat transfer coefficient was determined according to the local flow regime while the outer losses were evaluated by solving coupled energy balance equations for the absorber, glass envelope and secondary reflector using an iterative solver (*fsolve*). The wall temperature was updated iteratively until convergence, after which the local enthalpy was incremented based on the computed heat gain per unit length. The useful heat gain by the heat transfer fluid per unit length is equivalent to the convective heat transfer between the absorber tube's inner surface and HTF.

The thermal efficiency was computed using eq. (6) [10]:

$$\eta_{\text{therm}} = \left(\frac{Qu_{\text{total}}}{DNI \times A_{\text{p}} \times \eta_{\text{opt}}} \right) \tag{6}$$

where, Qu_{total} denotes the total useful heat gain (W).

Model validation. The model was validated using data reported in the literature, with key parameters, namely, mirror inclination, IAM and heat gain, benchmarked against the experimental results of Pino *et al.* [34] and Hafner *et al.* [37] for real LFR configurations. The validation process involved incorporating the geometric parameters and operating conditions of the experimental plant into the model and comparing the simulated outcomes with the experimental data. The discrepancies between the model results, experimental data and real LFR configuration were evaluated using the Coefficient of Determination (R^2) statistical method, computed using eq. (7) [38]:

$$R^2 = 1 - \frac{\sum_{i=1}^{n}(A_i - P_i)^2}{\sum_{i=1}^{n}(A_i - \bar{\text{E}}_i)^2} \tag{7}$$

where A_i denotes measured values, P_i denotes the predicted model values and $\bar{E}_i$ denotes the mean of measured values.

Individual optical loss components (blocking, shading and spillage) were not independently validated due to the absence of published experimental datasets reporting detailed geometric loss decomposition for identical LFR configurations. However, the adopted loss formulations are consistent with established analytical LFR optical models reported in literature.

Model assumptions. To aid the development of the model, several assumptions were made. The thermal model was based on steady-state conditions, ignoring potential transient effects. Additionally, a uniform circumferential heat flux distribution was assumed on the absorber's surface.

Although one-dimensional steady state formulation was employed, previous studies have demonstrated that such approaches can reliably predict receiver thermal performance, producing results consistent with experimental data. Liang *et al.* [36] compared one-dimensional models assuming uniform circumferential heat flux with more detailed formulations accounting for non-uniform flux and demonstrated that, while circumferential non-uniformities may induce localized wall temperature gradients, the differences in predicted outlet fluid temperature and overall thermal efficiency remain small. In the present configuration, the secondary reflector further enhances circumferential redistribution of reflected radiation, thereby reducing peak flux concentrations and temperature asymmetry on the absorber surface. Thus, while transient behaviour and local flux non-uniformities may occur under real operating conditions, their influence on overall thermal input is expected to be limited. Future work may incorporate transient and multi-dimensional modeling to enable refined prediction of local temperature fields and detailed thermal stresses.

System Optimization and Performance Analysis

The geometric solar field parameters and system size were optimized as outlined in Appendix A3.

Monthly performance analysis. A MATLAB simulation modelled the hourly energy flows of the LFR system integrated with storage and fuelwood backup, evaluating performance across six months: high irradiation months (January, February, December) and low irradiation months (April, May, October). The simulation accounted for continuous 24-hour factory operation, with monthly operational days adjusted accordingly. For each month, the hourly thermal energy demand was kept constant, with its value varying across months depending on respective monthly demand patterns. Hourly direct normal irradiance values were sourced from National Solar Radiation Database (NSRD) [39], while hourly optical and thermal efficiencies were calculated using the model developed in this study. The collector area was held constant throughout the simulations. Also, the thermal storage capacity was not treated as an independent design variable but was coupled to the optimized solar field size within the system optimization framework. It, therefore, remained fixed during the analysis.

The algorithm operates through nested temporal loops, progressing from months to days to hours, to replicate energy dispatch priorities while accounting for system constraints. At the start of each monthly cycle, the storage state of charge (*SOC*) is reset to zero and hourly, location-specific *DNI* and efficiency data are processed. Solar generation is prioritized to meet process demand, with surplus energy directed to thermal storage subject to capacity constraints, and any excess dissipated. During deficits, the system first deploys stored energy, accounting for discharging losses; followed by dispatch of a fuelwood-fired boiler, treated as a load-following backup. This hierarchy maximizes renewable utilization while ensuring operational reliability under varying irradiation conditions. A flowchart of the simulation process is presented in Figure 3.

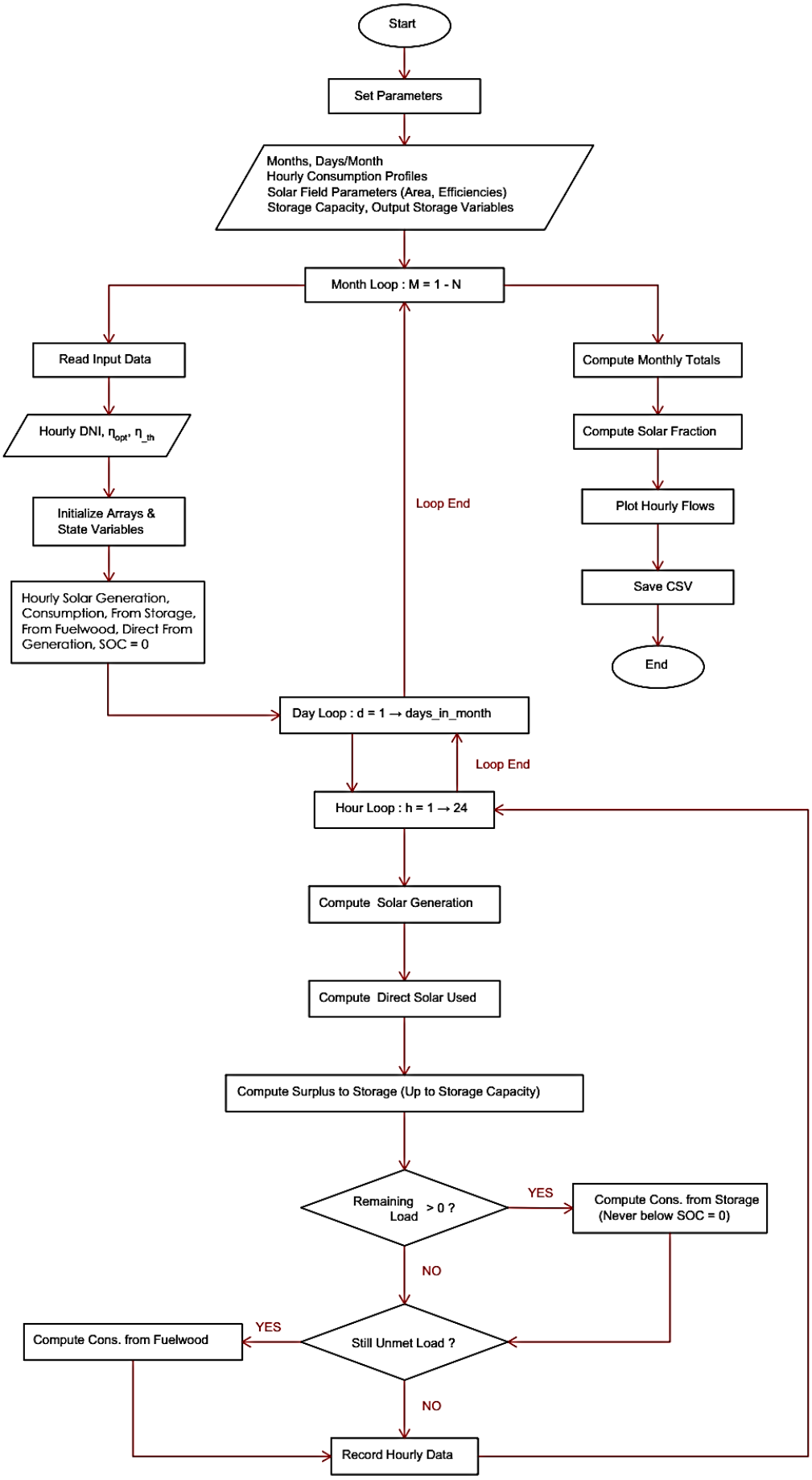

Figure 3. Flowchart of hourly energy flow simulation

The hourly dispatch algorithm assumes idealized priority-based control without explicitly modeling actuator response times, valve dynamics, or ramp-rate constraints of the storage and back-up systems. Energy flows are resolved at an hourly time step, and switching between solar, storage and fuelwood sources treated as instantaneous within each time interval. This approach captures system-level energy balances while neglecting short duration transient control effects occurring at sub-hourly time scales. Incorporating detailed dynamic control modeling would increase computational complexity and require additional system-specific control parameters. Future work may integrate transient control simulation to quantify short term operational effects and refine dispatch predictions.

The simulation outputs include monthly solar energy generated, energy supplied from storage, and energy supplied from fuelwood boiler system. In addition, the solar fraction – a key performance metric – is calculated monthly to capture the system's responsiveness to seasonal irradiation patterns. The hourly solar energy generated was computed using eq. (8):

$$h_{\text{thg}} = DNI \times h \times A_{\text{c}} \times \eta_{\text{th}} \times \eta_{\text{opt}} \tag{8}$$

where *DNI* denotes the hourly direct normal irradiance (MW/m^2), h denotes the number of hours (set to 1), A_{c} denotes the total collector area in (m^2), η_{opt} and η_{th} represent collector's hourly optical and thermal efficiencies, respectively.

The charging and discharging efficiencies were set at 0.99 [40] while the distribution system efficiency was set at 0.85.

Environmental impact assessment. The reduction in CO_2 emissions resulting from partial displacement of fuelwood was quantified using an emission factor of 2.27 kg CO_2 per kg MT reported for Kenyan tea factories [16], [17]. Baseline factory data indicate that an annual production of 3,450,000 kg MT requires approximately 11,500 trees [18]. These values were used as reference case. The annual solar fraction was determined as the average of the representative high and low irradiation months obtained from the dynamic hourly simulations. The corresponding reduction in annual fuelwood contribution was then applied proportionally to the baseline tree consumption and associated emissions.

Economic Analysis

The economic analysis of the optimized linear Fresnel reflector system was conducted using four key performance indices: levelized cost of heat (*LCOH)*, internal rate of return (*IRR*), net present value (*NPV*), and simple payback period (*SP*), computed using eq. (9) to eq. (14) [41], [42]:

$$LCOH = \frac{\gamma_{\text{a}}}{E_{\text{annual,thermal}}} \tag{9}$$

$$\gamma_{\text{a}} = (K_{\text{a}} + K_{\text{i}} + K_{\text{O\&M}})\,\gamma_{\text{Total investment}} \tag{10}$$

$$\gamma_{\text{Total investment}} = (1 + K_{\text{u}})\left[(1 + K_{\text{e}})\left(C_{\text{c}}^{\text{d}}\right) + C_{\text{l}}A_{\text{T}}\right] \tag{11}$$

$$NPV = \sum_{t=0}^{N} \frac{Revenue_t - Cost_t}{(1+d)^t} \tag{12}$$

$$IRR: NPV = \sum_{t=0}^{N} \frac{Revenue_t - Cost_t}{(1+d)^t} = 0 \quad (13)$$

$$SP = \frac{Capital\ expenditure}{Annual\ LFR\ revenue - O\&M} \quad (14)$$

where: γ_a is the annualized plant cost (USD), $E_{annual,thermal}$ is the collected annual solar energy (J), K_a is the annuity factor (%), K_i is the insurance (%), $K_{O\&M}$ is the operation and maintenance (%), $\gamma_{Total\ investment}$ is the total investment (USD), K_u is the uncertainties (%), K_e is project efforts, C_c^d is the direct costs (USD/m^2), A_T is the total ground area (m^2), C_l is the land acquisition & preparation cost (USD/m^2), N is the period of analysis (years), d denotes discount rate, t denotes time variable in every computation, $Revenue_t$ denotes LFR system returns in period t, $Cost_t$ is the system cost at year t.

The constant parametric factors used to estimate the indirect costs are summarized in **Table 2**.

Table 2. LFR indirect cost parameters [41]

K_u	5%
K_e	22.5%
K_a	9.368%
K_i	1%
$K_{O\&M}$	2%

The economic analysis was conducted over a 25-year period, as recommended by Ordóñez *et al.* [41] . The LFR cost estimates were sourced from Khajepour & Ameri [43] as presented in **Table 3**.

Table 3. LFR system cost parameters [43]

Solar Field & Storage	
Direct Costs (DC)	
Site improvement (USD/m^2)	20
Solar Field (USD/m^2)	170
HTF system (USD/m^2)	40
Thermal Storage System (USD/kWh$_t$)	77
Contingency	10 % of total *DC*
Indirect Costs	
Design & Construction	11% of total *DC*
Land cost (USD/m^2) (*site specific*)	7.63

Economic indicators relevant to Kenya were considered, including an annual average inflation rate of 5.14% [44], an import duty of 25% [45], a Value Added Tax (VAT) of 16% [46], and an interest rate of 12.75% [47].

A deterministic sensitivity analysis was performed around the optimal configuration to quantify the impact of key uncertainties on *LCOH*, *NPV* and *IRR*. *DNI* was varied by ±4% [39], thermal efficiency by ±6%, capital expenditure by ±5% [41], *O&M* costs by ±5% [41]. Furthermore, to assess the generalizability of the economic results, a macroeconomic sensitivity analysis was conducted around the optimal configuration. The analysis varied key

financial parameters based on their observed 10-year historical ranges in Kenya: interest rate (±4.25%), inflation (±4.51%) and VAT (±2%) [46], [47]. Each parameter was varied independently while the remaining performance and economic inputs retained their respective base-case values as previously computed.

RESULTS AND DISCUSSION

This section presents the study findings, covering the factory's energy demand, climatic and solar resource assessment, model validation, solar field optimization, system performance during low and high *DNI* months, economic feasibility and environmental implications of LFR adoption in the Kenyan tea industry, followed by a detailed discussion.

Climate and Energy Demand at Momul Tea Factory

Figure 4 illustrates the study location's solar resource and climatic conditions over the year. The average ambient temperature ranges from 16.6 °C in July to 18.8 °C in March. Wind speeds are generally low, varying between 1.6 m/s in May, June and July and peaking at 2.6 m/s in February at a height of 10 m [48]. The December – February season experiences high direct normal irradiation levels, peaking at 6.89 kWh/m^2/day in December. Conversely, April, May and October are characterized by high solar resource intermittency, with October receiving the lowest direct normal irradiation level of 4.15 kWh/m^2/day. The cumulative annual direct normal irradiation is 1915.59 kWh/m^2 [25]. Solar thermal linear focusing technologies are promising in regions with direct normal irradiation values exceeding 4.0 kWh/m^2/day and total annual direct normal irradiation values above 1600 kWh/m^2 [49], [50]. Therefore, the study location receives sufficient direct normal irradiation to support LFR systems.

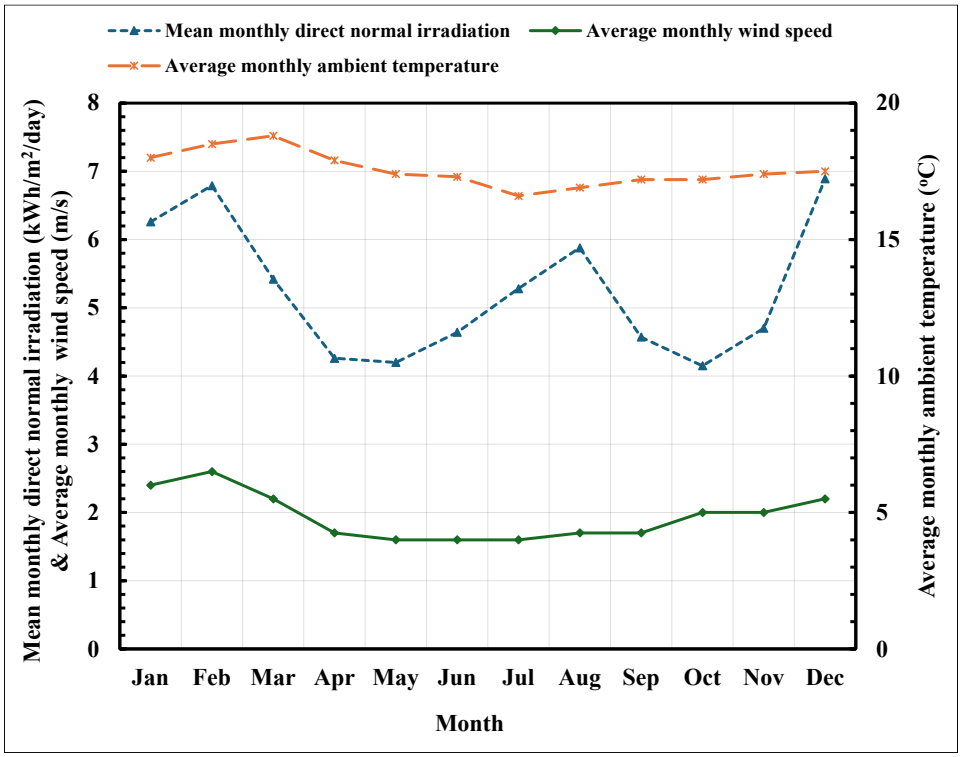

Figure 4. Mean monthly direct normal irradiation, ambient temperature and wind speed [48]

Figure 5 shows the trends in thermal energy demand over the year. Tea production and thermal energy demand follow similar trends. January records the highest tea production of 441,412 kg while February recorded the lowest production of 240,841 kg. Similarly, the peak

thermal energy demand of 1,686 MWh is observed in January while the lowest demand of 920 MWh occurs in February. The total annual thermal energy demand is 17,430 MWh.

Fuelwood is combusted in a boiler to generate steam at a pressure of 8 bar, a temperature of 170 °C and a flow rate of 4,065 kg/h. After the steam is utilized, the condensate is recovered and redirected to a heat exchanger, where it is used to preheat the feed water to a temperature of 87 °C. On average 1 m^3 of fuelwood costs KES 3,000 and generates 1,792 kg of steam, which is used to produce 261 kg MT.

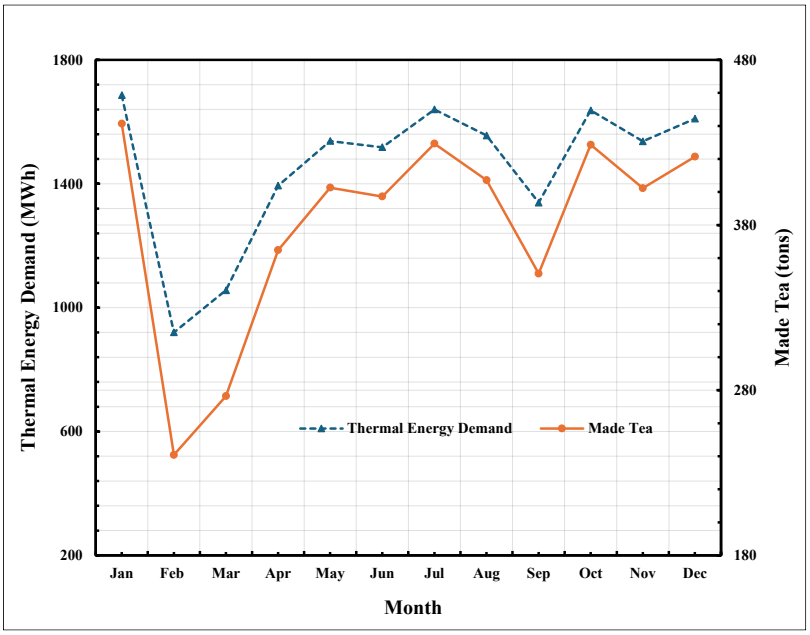

Figure 5. Monthly thermal energy demand and tea production at Momul Tea Factory

Model Validation Results

Figure 6 illustrates the model validation with published experimental data. From **Figure 6a**, the inclination values predicted by the model exhibit a high degree of correlation with the values across all the three time slots as measured by Pino *et al.* **[34]**. The maximum deviation is 0.4°, with R^2 values of 0.9995, 0.9995 and 0.9997 for 1 PM, 2 PM and 3 PM time slots, respectively. Similarly, in **Figure 6b**, the model closely matches the incidence angle modifiers (IAM) from Hafner *et al.* **[37]** in both transversal and longitudinal directions. Since Hafner *et al.* present IAM values for 4, 8 and 16 modules, only the four-module results are used for validation in this study. For the transversal case, the R^2 value is 0.997, with a slight underprediction between 25° and 45°. The longitudinal case also achieves a strong overall fit with an R^2 value of 0.983, with the model slightly overestimating performance between 35° and 70° but still capturing the characteristic decay across the angular range.

In **Figure 6c**, the model predictions for the total heat gain by the heat transfer fluid (HTF) match closely with the measured values across all the six time slots with an R^2 value of 0.9561. The maximum deviation between the model and measured total heat gain by HTF was 3.8 kW at 3:30 PM. The beam radiation incident on the receiver dictates the overall heat gain profile. From 13:00 to 14:00, the radiation levels are relatively high and stable (ranging between 148.9 kW and 152.3 kW), corresponding with the increasing trend in the heat gain by the HTF. After 14:00, a sharp drop in beam radiation is observed, reaching a minimum of 88.5 kW at 15:00. This decline is mirrored by a pronounced drop in both the calculated and measured heat gain, reflecting the system's response to diminished solar input. The model and measured outlet fluid temperatures also exhibit a high degree of agreement, with R^2 values of 0.9790. The maximum deviation between the calculated and measured outlet temperatures was 2.7 °C at 2 PM.

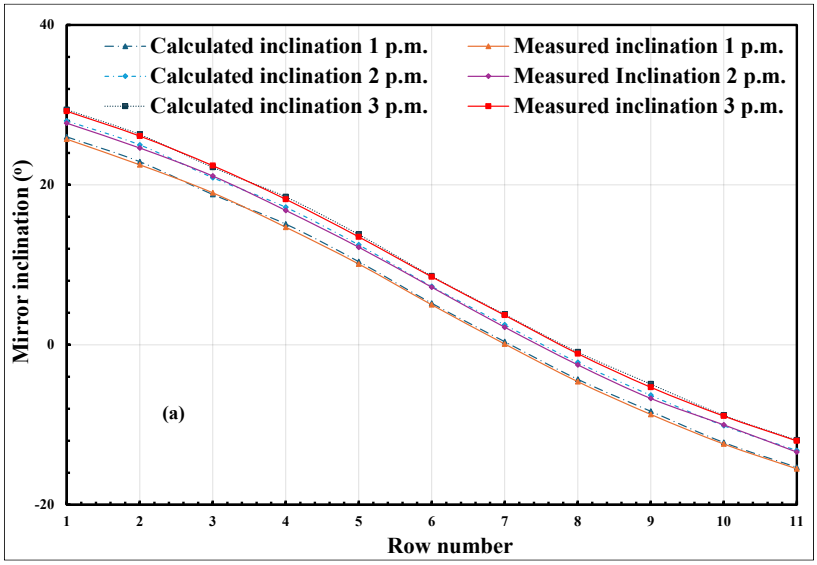

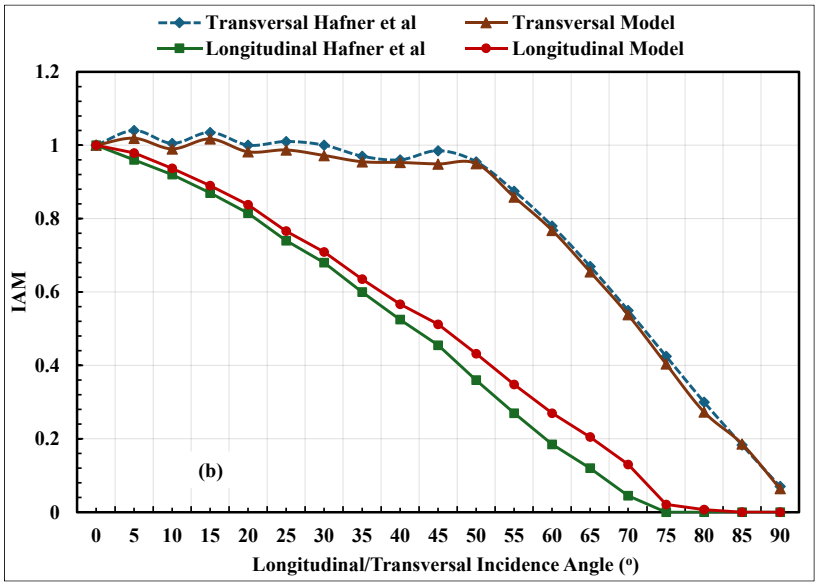

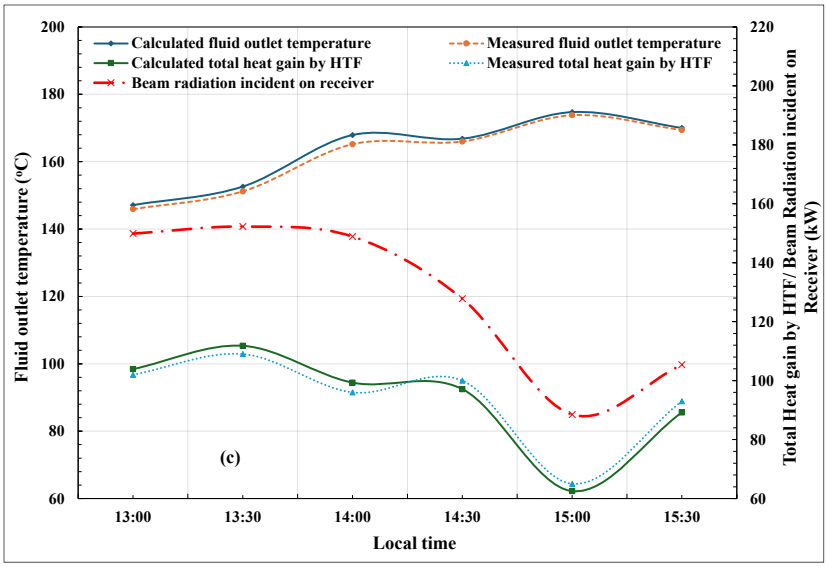

Figure 6. Validation of the model with other studies: (a) Mirror inclination, (b) Incidence angle modifier and (c) Fluid outlet temperature and total heat gain

Optimization Results

Optimal parameters. **Table 4** presents the optimized geometric parameters of the solar field – including receiver height, mirror width and row spacing – along with the corresponding optical efficiency.

Table 4. Optimized parameters

Parameter	Optimal value
Receiver height	4.4 m
Mirror width	0.5 m
Row spacing	0.2 m
Optical efficiency	66.28%

Figure 7 presents the two-dimensional contour plots that provide a sensitivity-based assessment of the optimized configuration, showing how optical efficiency varies with small deviations from the optimal design parameters. The contour plot of receiver height and mirror width in **Figure 7a** exhibits a single peak centered near a receiver height of 4.4 m and mirror width of 0.5 m, respectively. The contours form approximately elliptical patterns around the optimum, indicating a unique global solution. Below 4.4 m, the optical efficiency increases rapidly with receiver height due to reductions in shadowing, blocking of reflected radiation and spillage losses. Beyond 4.4 m, the contours become more widely spaced in the height direction, indicating reduced gradient magnitude and greater tolerance to further height increases. In contrast, tighter contour spacing for mirror widths exceeding 0.5 m reflects stronger sensitivity to aperture enlargement, where increased shading of adjacent reflectors and blocking of reflected radiation outweigh gains in reflective aperture area.

Similarly, the mirror width – row spacing contour in **Figure 7b** demonstrates a pronounced peak at approximately 0.5 m and 0.2 m. Optical efficiency increases rapidly as row spacing approaches 0.2 m from the lower values due to reduced inter-row shading but declines sharply beyond this point as reflected radiation increasingly misses the receiver. The comparatively dense contour spacing along the row spacing axis indicates higher sensitivity to spacing variations relative to mirror width.

The receiver height-row spacing contour in **Figure 7c** further confirms broader tolerance in receiver height compared to row spacing, particularly above the 4.4 m optimum. Optical efficiency rises steadily with height up to 4.4 m and decreases more gradually thereafter, whereas row spacing exhibits steeper gradients on both sides of 0.2 m.

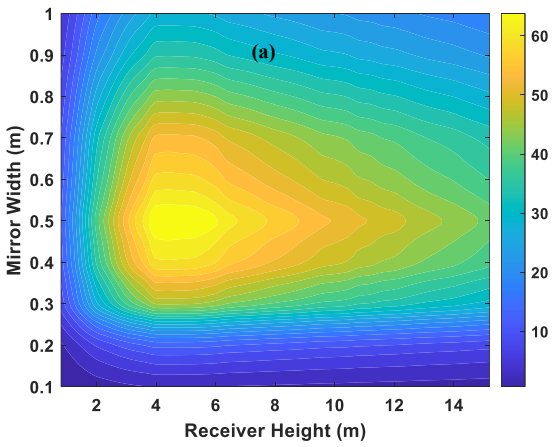

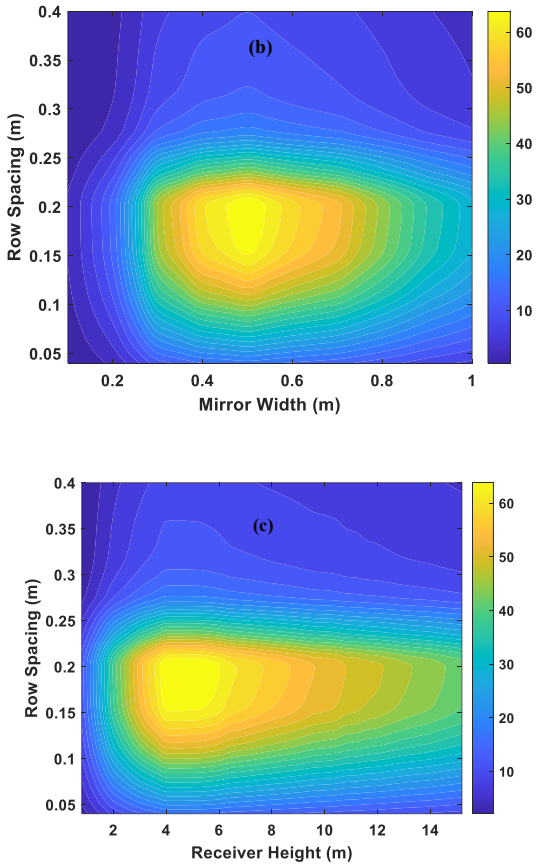

Figure 7. Optical efficiency contour plots: (a) Receiver Height vs Mirror Width, (b) Mirror Width vs Row Spacing, and (c) Receiver Height vs Row Spacing

Overall, the contour topology provides insight into the response surface of the objective function. Receiver height primarily controls interception efficiency and ground clearance effects, while mirror width and row spacing strongly influence inter-mirror shading and reflected beam divergence. The smooth contour regions surrounding the optimum indicate a stable global solution within the defined design space. A comparison with previous studies, summarized in **Table 5**, reveals both consistencies and variation in the optimization trends.

Table 5. Comparison with previous studies

Receiver Type	**Optimized parameters**				**Study**
	***W* (m)**	***H* (m)**	***S* (m)**	**Optical efficiency (%)**	
Evacuated tube	0.4 – 0.5	4 (fixed)	0.06 – 0.25	58.2 – 63.41	Ajdad *et al.* [51]
Evacuated tube	0.25	11.81	-	60.29	Cheng *et al.* [52]
Multi-tube cavity	0.68	-	-	-	Moghimi *et al.* [24]
Multi-tube cavity	0.28	2.3	-	-	Pulido-Iparraguirre *et al.*, [12]
Trapezoidal cavity	0.48 – 0.52	8 (fixed)	-	-	Roostaee & Ameri [53]
Evacuated tube	**0.5**	**4.4**	**0.2**	**66.28**	**Current Study**

There are notable similarities between the results of this study and those reported in previous works with respect to mirror width and row spacing, which generally fall within the ranges of 0.4 – 0.5 m and 0.06 – 0.25 m, respectively. The consistencies reinforce the validity of the presented model. However, a significant discrepancy is observed in the optimized receiver height. While reported optimal heights reach up to 11.81 m, the present study yields a lower optimal height of 4.4 m for a medium-sized collector. This variation reflects both the collector scale and the adopted optimization methodology. In this study, the receiver height is optimized simultaneously with mirror width and row spacing, capturing the interplay among these parameters, which significantly influences optimal system performance.

In general, the identification of optimal parametric setpoints ensures a balanced system design that maximizes the optical efficiency by minimizing shading, blocking, and spillage.

The MATLAB-based simulation results for the evacuated tube receiver are presented in **Figure 8**. The inlet HTF and ambient temperatures were maintained at 87 °C and 18 °C, respectively. As the HTF outlet temperature increases from 100 °C to 300 °C, the thermal efficiency decreases gradually from 65.05% to 62.6%. However, beyond 300 °C, thermal efficiency drops steeply, reaching 58.51% at 400 °C. In contrast, the heat loss per unit length rises significantly with increasing outlet temperature, from 22.76 W/m at 100 °C to 219.76 W/m at 400 °C. This inverse relationship indicates that as the outlet temperature increases, convective and radiative heat losses become more pronounced, leading to a marked reduction in thermal efficiency. The sharp decline beyond 300 °C underscores the dominant influence of the temperature-dependent radiation losses at elevated fluid outlet temperatures.

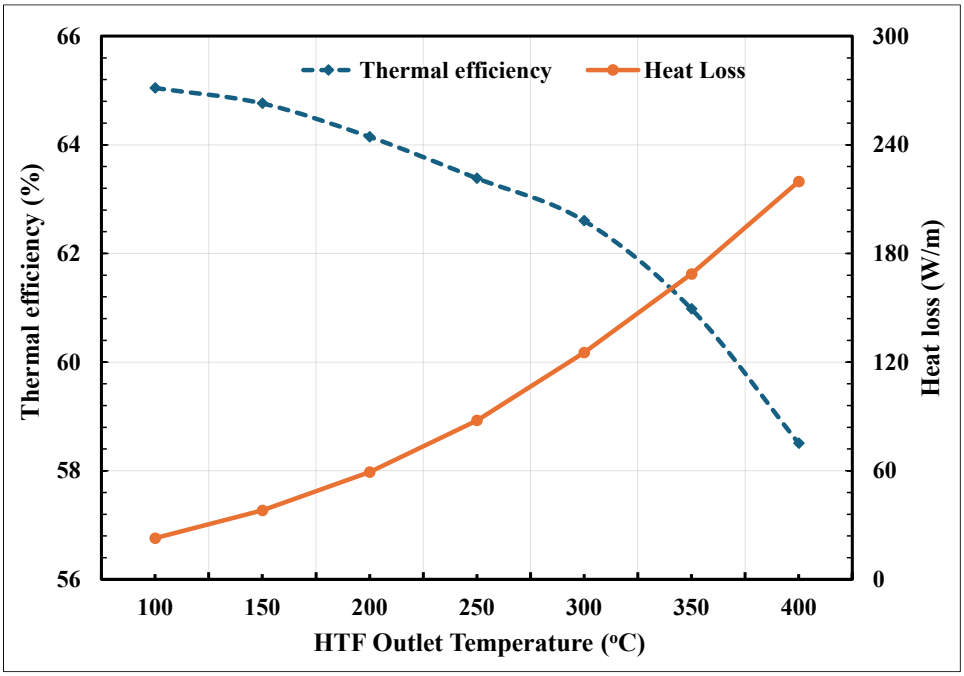

Figure 8. Influence of heat transfer fluid outlet temperature on LFR receiver's heat loss per unit length and thermal efficiency

Linear Fresnel Reflector System Size. An average daily thermal energy demand of 56 MWh serves as the benchmark to evaluate the capability of each system size in meeting the energy requirements. **Figure 9** illustrates the influence of solar multiple on solar energy generated and solar fraction. The solar field area ranges between 7680 m^2 and 23,040 m^2 as SM increases from 1 to 3. From **Figure 9a**, at a *SM* of 1, the system only meets the 26 MWh demand during sunny hours. For solar multiples between 1.25 and 2, the system meets the demand during sunny hours while storing 7.39 – 27.47 MWh of the 30 MWh nighttime demand. At *SM* 2.25, the system generates a total of 60.86 MWh, marginally exceeding the

daily demand. The stored 34.86 MWh fully meets nighttime demand and offers a 4.86 MWh buffer for variability. Between *SM* 2.5 and 3, the system produces a surplus for storage, increasing from 41.2 MWh to 54.93 MWh, with equivalent storage hours varying between 17 and 22.

Secondly, achieving 100% solar fraction is crucial for maximizing the substitution of fuelwood. **Figure 9b** shows that at SM values of 2 or lower, the solar field area is insufficient to meet this target. *SM* 2.25 marginally exceeds this target. When *SM* exceeds 2.25, *SF* significantly exceeds 100%, indicating a system overdesign for fuelwood substitution. Therefore, optimal system features a *SM* of 2.25, 1.03 SF and an area of 17,280 m^2, striking a balance between maximizing fuelwood substitution and minimizing the solar field size.

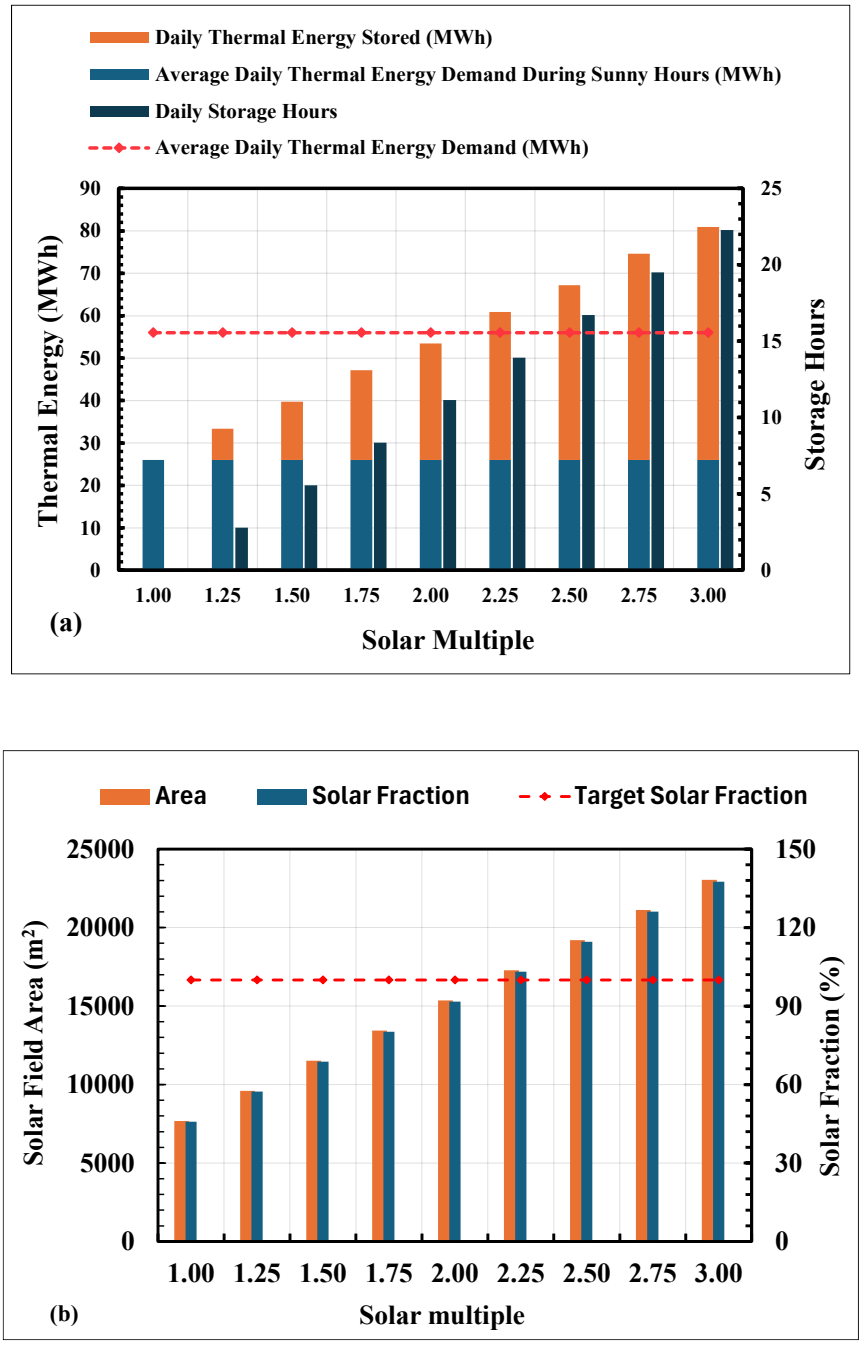

Figure 9. Influence of solar multiple on (a) thermal energy generated and stored thermal energy and (b) solar field size and solar fraction

The technical specifications of the LFR plant are detailed in **Table 6**.

Table 6. Technical specifications of the LFR plant

Parameter	Value
Reflective area	17,280 m^2
Thermal energy storage technology	Ruth's Accumulator
Thermal energy storage capacity	34.86 MWh
Steam accumulator volume	92 m^3
Charging Pressure	12 bar
Discharging Pressure	8 bar
Feed water inlet temperature	87 °
Steam flow rate	4065 kg/h

Performance analysis of optimized system

Figure 10 presents the detailed hourly energy flows for each of the selected months, illustrating the dynamic interplay between solar energy generation, storage dispatch and fuelwood contribution.

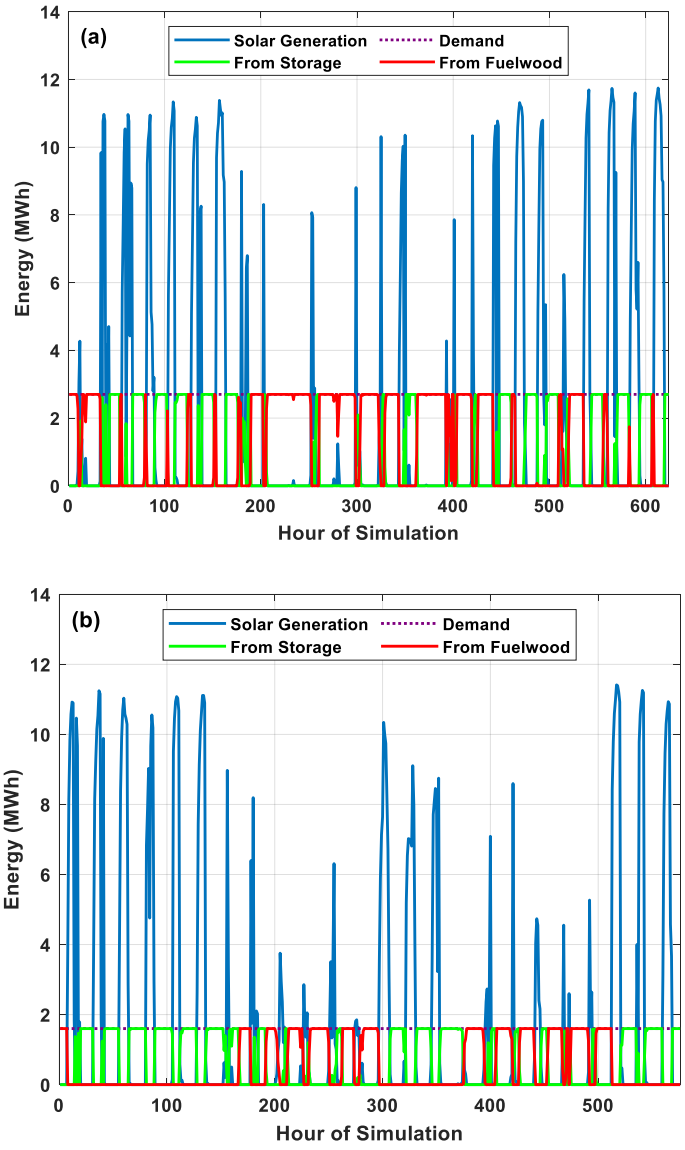

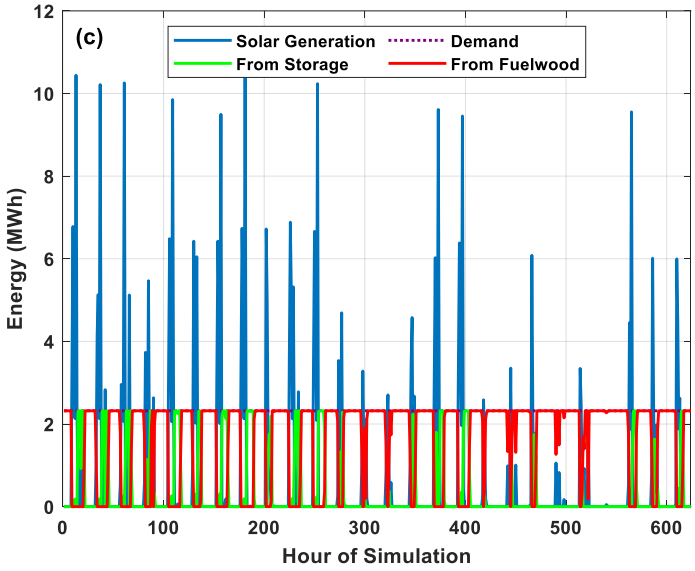
(c)
Solar Generation
Demand
From Storage
From Fuelwood
Energy (MWh)
Hour of Simulation

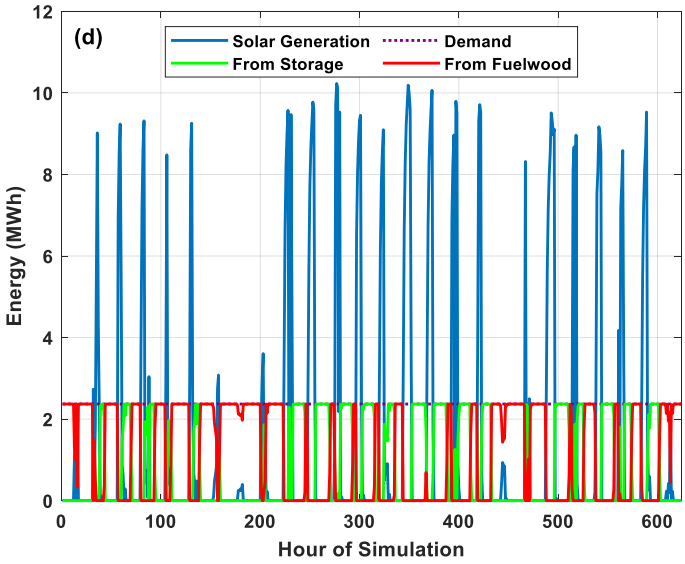
(d)
Solar Generation
Demand
From Storage
From Fuelwood
Energy (MWh)
Hour of Simulation

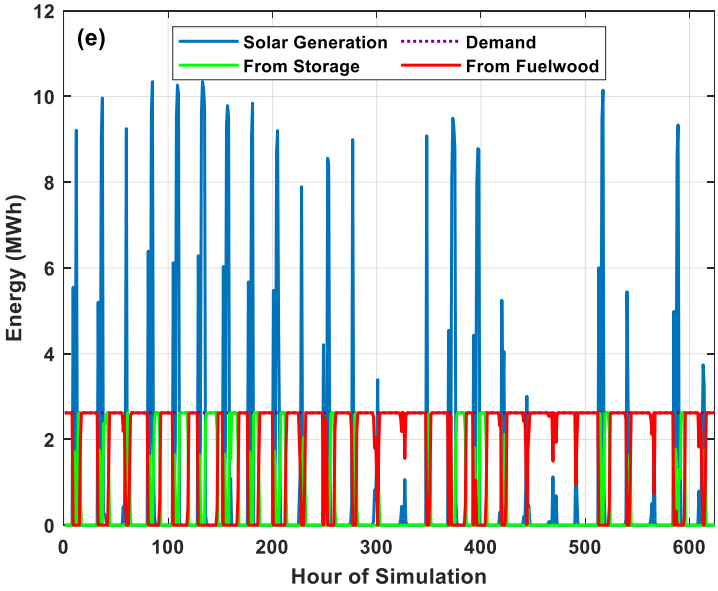
(e)
Solar Generation
Demand
From Storage
From Fuelwood
Energy (MWh)
Hour of Simulation

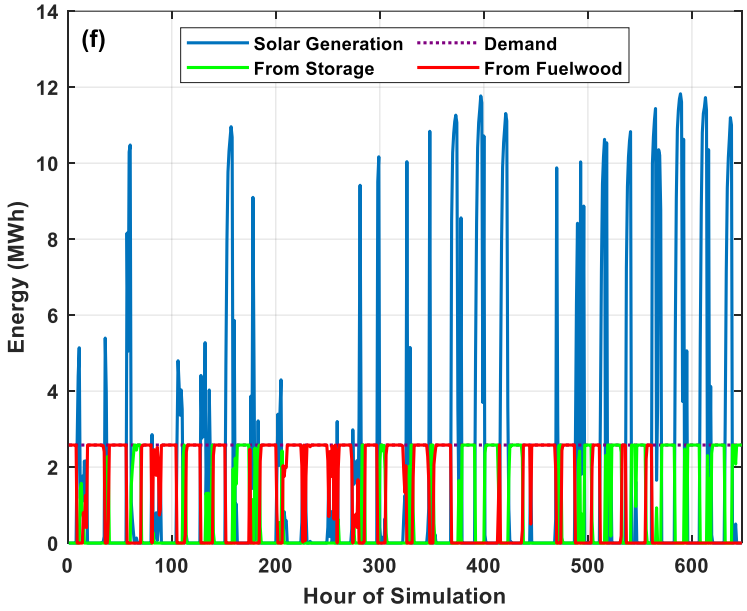

Figure 10. Hourly energy flows for selected months: (a) January, (b) February, (c) April, (d) May, (e) October, and (f) December

Table 7 quantifies monthly performance, enabling direct comparison of solar utilization across seasons.

Table 7. Monthly Energy Summary

Month	Demand (MWh)	Direct from Solar plant (MWh)	From Storage (MWh)	From Fuelwood (MWh)	Solar Fraction
January	1684.8	411.07	540.35	733.39	0.5647
February	921.6	252.87	373.41	295.31	0.6796
April	1447.7	246.12	195.24	1006.3	0.3049
May	1478.9	304.87	486.95	687.06	0.5354
October	1634.9	227.11	289.08	1118.7	0.3157
December	1671.8	406.66	479.95	785.23	0.5303

The results demonstrate clear seasonal patterns, with solar fractions ranging from 0.5303 to 0.6796 during high irradiation months (January, February, December) compared to a range of 0.3049 to 0.5354 in low irradiation months (April, May, October). February recorded the best performance, with the favorable solar conditions and moderate demand (921.6 MWh) allowing the LFR system to meet 67.96% of the factory's energy demand. April represented the system's most challenging scenario, with fuelwood supplying 69.59% of the 1447.7 MWh demand due to constrained solar availability.

The storage system's critical role in mitigating intermittency while enhancing solar energy penetration becomes evident when examining monthly performance variations. During January and December, months with similar high demand – 1684.8 MWh and 1671.8 MWh – storage contributions of 540.35 MWh and 479.95 MWh respectively maintained solar fractions above 0.53. However, the system's ability to leverage storage was fundamentally constrained during low-irradiation periods by insufficient charging opportunities as evidenced by April's modest 195.24 MWh storage contribution. This directly correlated with increased fuelwood dependence, which peaked at 1118.7 MWh (68.4% of demand) in October. The average solar

fraction in high irradiation months (0.5915) is about 1.5 times that of low irradiation months (0.3853), highlighting the system's strong sensitivity to seasonal variations in direct solar availability. The schematic of the hybrid system is illustrated in **Figure 11**.

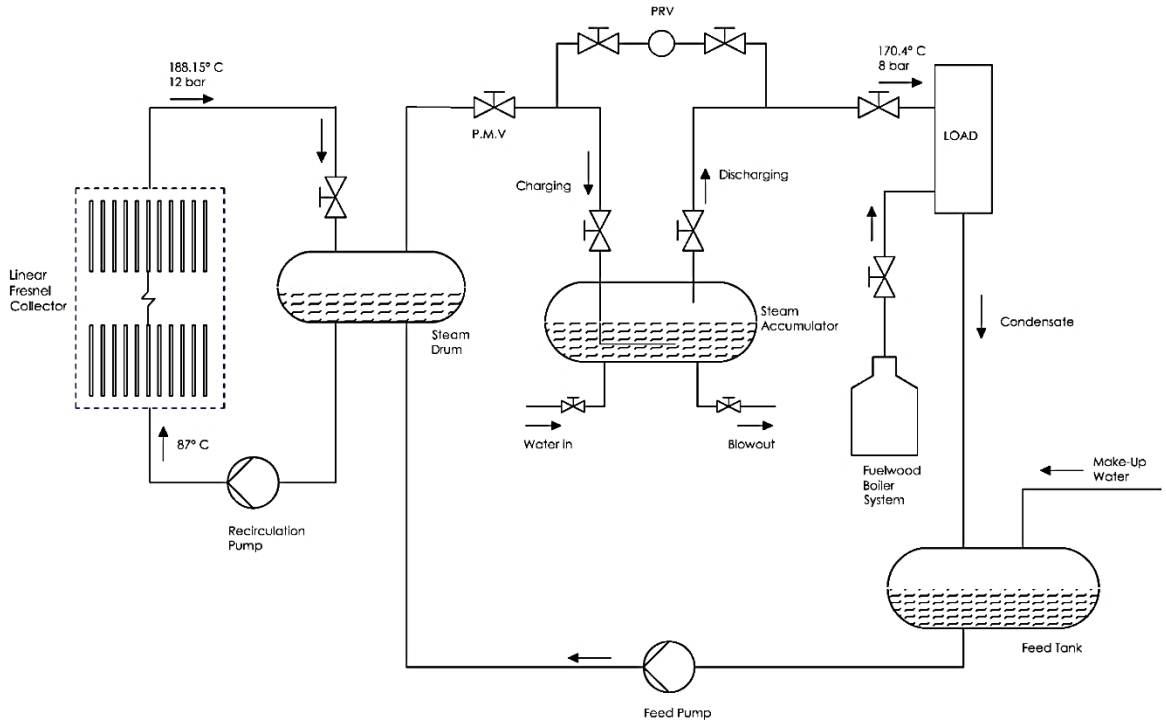

Figure 11. Hybrid system schematic

In practical operation, system performance may also be influenced by control dynamics such as valve response times, thermal inertia of the receiver and piping network, storage and discharging power limits and boiler ramp-rate constraints. During periods of rapidly fluctuating *DNI*, these factors can delay charging or discharging responses, potentially reducing effective solar utilization and increasing short-term reliance of fuelwood backup system. Consequently, real plant operation may achieve marginally lower instantaneous solar fractions than those predicted under the ideal dispatch consideration adopted in the hourly model. However, since industrial thermal demand varies relatively slowly and thermal storage provides buffering capacity, these short-duration deviations are unlikely to significantly alter aggregated monthly energy balances or the overall seasonal performance trends.

From those results, although the system is designed to achieve a *SF* of 1 based on the average daily thermal energy consumption over the year, performance analysis of hourly energy flows of six select months highlights the need of hybridizing the system with fuelwood to ensure continuous energy supply. Fuelwood would contribute to 40.85 % and 61.47 % of the demand during high and low *DNI* months, respectively. The Momul tea factory consumes 17,450 trees from 24.93 acres, resulting in approximately 10,358 metric tons of CO_2 emissions annually. The hybrid system would require 7,782 trees from 10.83 acres annually, achieving a 48.84% reduction in both tree consumption and CO_2 emissions. This significant improvement helps in reducing deforestation and enhances sustainability in the tea industry.

Economic Analysis of the Linear Fresnel Reflector System

For its exclusive use of fuelwood for thermal energy supply, the factory consumes about 17,450 m^3 of fuelwood annually at a cost of KES 53,274,807. Based on the current exchange rate provided by the Central Bank of Kenya **[54]**, this equates to 412,983 USD, resulting in a levelized cost of heat (*LCOH*) of 2.49 cUSD per kWh.

Figure 12 illustrates the economic performance of various LFR system sizes. **Figure 12a** shows that both *LCOH* and payback period generally increases with higher solar multiples. At SM 1, the system achieves the lowest *LCOH* of 1.84 cUSD/kWh and the shortest payback period of 6.02 years, highlighting favorable economic performance at smaller solar field sizes. However, as the solar multiple increases, the incremental investment outweighs additional energy benefits, leading to higher *LCOH* values and extended payback durations. At SM 2.25, the *LCOH* is 3.04 cUSD/kWh while the payback period is 8.9 years, beyond which further increases result in diminishing economic returns.

Figure 12b reinforces this trend through *NPV* and *IRR*. At lower solar multiples, *NPV* is strongly positive, but it decreases steadily and becomes negative at higher values. Similarly, *IRR* declines with increasing SM, with a sharper reduction at lower values that lessens at higher multiples, reflecting diminishing marginal returns. The financial viability threshold occurs at *SM* 2.25 where *NPV* is 1,288 USD and *IRR* is 12.78%, above the prevailing interest rate of 12.75% [47]. Beyond this point, *NPV* turns negative, and *IRR* falls below the prevailing interest rate, indicating that solar multiples greater than 2.25 are economically unattractive.

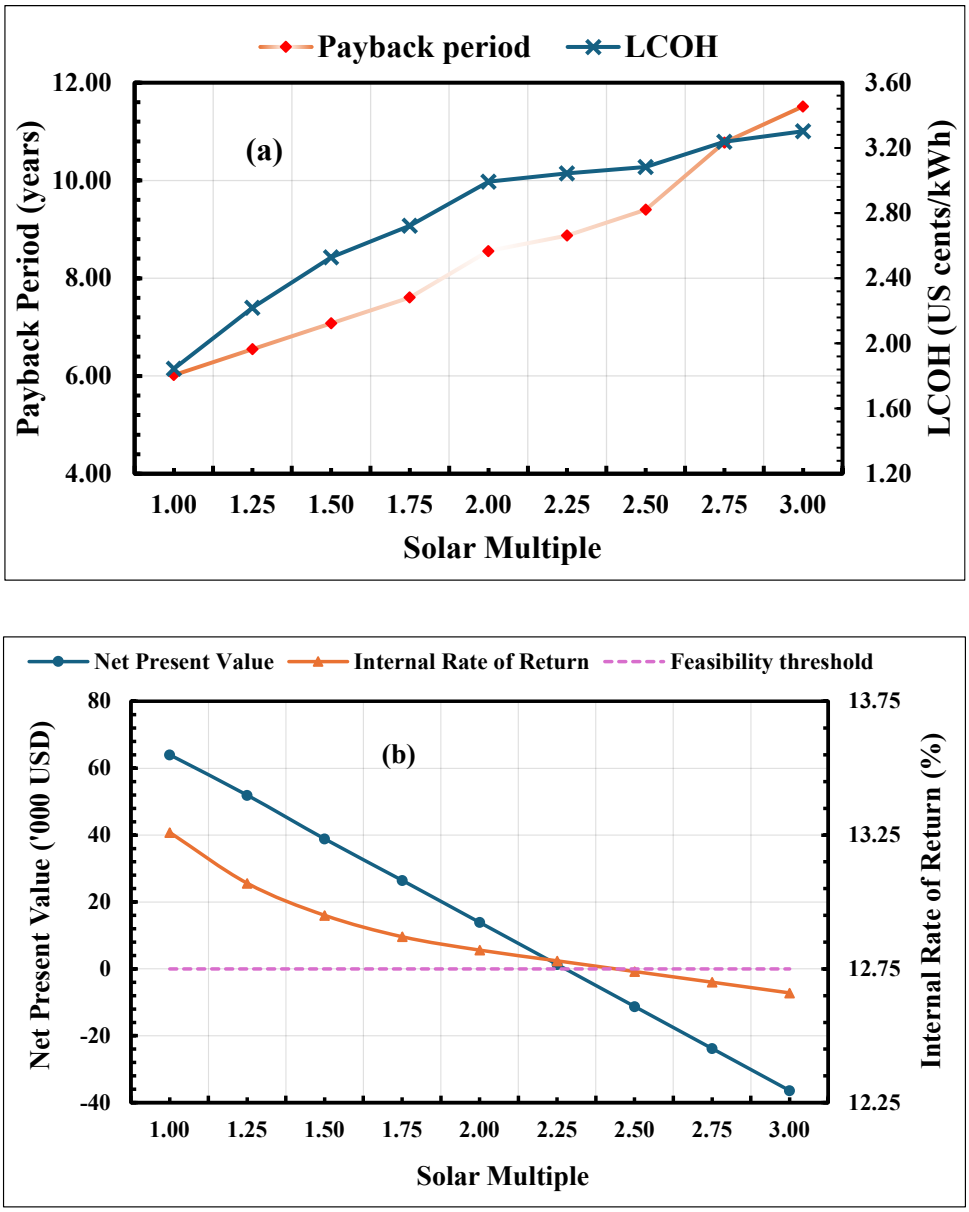

Figure 12. Economic performance indices: (a) payback period and levelized cost of heat and (b) net present value and internal rate of return

Uncertainty analysis. **Table 8** shows the sensitivity of economic indicators to the variation of performance and cost inputs for the optimal configuration (*SM* = 2.25). Results indicate that *LCOH* varies proportionally with capital expenditure (±5%). Variations in *DNI* and thermal efficiency produce an inversely proportional change in *LCOH* due to its direct influence on annual thermal energy yield. *NPV* is most sensitive to capital expenditure, exhibiting approximately ∓25% variation for ±5% change in capital expenditure, reflecting the influence of upfront investment on long-term cash flow. *O&M* cost variations exert moderate influence on *NPV*, while *DNI* and thermal efficiency variations produce smaller *NPV* shifts, with ±4% and ±6% variations occasioning ±5% and ±7% changes, respectively. *IRR* shows comparatively limited sensitivity, all within ±2%, remaining close to but above the prevailing interest rate under the tested uncertainty bounds. Overall, the system retains economic feasibility under realistic variations in solar resource, performance and cost parameters, although capital expenditure remains the dominant economic risk factor.

Table 8. Sensitivity of Economic Indicators to performance and cost inputs

Parameter	**Variation**	***LCOH* change**	***NPV* change**	***IRR* change**
DNI	±4%	∓4%	±5%	±0.12%
Thermal efficiency	±6%	∓6%	±7%	±0.18%
Capital Expenditure	±5%	±5%	∓25%	∓0.20%
O&M cost	±5%	±2%	∓8%	∓0.08%

Table 9 shows the sensitivity of economic indicators to the variation of key financial parameters for the optimal configuration (*SM* = 2.25). The results indicate that *NPV* is particularly sensitive to variations in interest rate. Since the optimized configuration yields a marginal baseline *NPV* (1,288 USD), ±4.25% changes in the interest rate produce comparatively large relative shifts (∓30%) in *NPV* over the 25-year analysis period. Higher interest rates substantially reduce discounted cashflows, thereby compressing profitability margins, while lower financing costs improve economic attractiveness. The variations also occasion a ∓6.9% change in *LCOH* and ∓1.8% change in *IRR*, indicating that financing conditions materially influence both cost competitiveness and investment performance. At an elevated interest rate of 17%, the *IRR* decreases to 12.55%, falling below the baseline financing threshold and rendering the project economically unattractive under such borrowing conditions. VAT variations primarily affect capital expenditure and therefore induce modest shifts in *LCOH* and *NPV*. ±2% VAT variation occasions ∓1.97% and ∓4.96% changes in *LCOH* and *NPV*, respectively. However, given the marginal profitability of the optimized configuration, even small capital cost adjustments translate to measurable changes in *IRR*, reinforcing the sensitivity of this configuration to fiscal policy parameters. Inflation predominantly influences long-term operating cost escalation and revenue progression over the 25-year analysis period. Within the tested ±4.51% range, inflation variations result in approximately ∓4% change in *LCOH* and ∓10% in *NPV* (1,159 – 1,417 USD). The associated *IRR* varies by approximately ∓0.35%, yielding a range of 12.43% to 13.13%. While these variations are less pronounced than those occasioned by interest rates fluctuations, higher inflations slightly compress long-term profitability by reducing cash flow margins.

Table 9. Sensitivity of economic indicators to financial parameters

Parameter	Range considered	*LCOH* (cUSD /kWh)	*NPV* ('000 USD)	*IRR* (%)
Baseline	-	3.04	1.288	12.78
Interest rate	8.5 – 17%	2.83 – 3.25	0.902 – 1.674	12.55 – 13.01
VAT	14 – 18%	2.98 – 3.10	1.224 – 1.352	12.73 – 12.83
Inflation	0.63 – 9.65%	2.92 – 3.16	1.159 – 1.417	12.43 – 13.13

Overall, the analysis demonstrates that while optimized *LFR* configuration remains economically viable under moderate macroeconomic fluctuations, its marginal *NPV* makes it particularly sensitive to financing conditions. These findings underscore the importance of stable borrowing environments and supportive financial frameworks in enhancing the attractiveness of industrial solar thermal systems.

CONCLUSIONS

This study presents a comprehensive modeling, optimization and economic evaluation framework for a medium-temperature *LFR* system designed for direct steam generation in a Kenyan tea factory. Distinct from prior studies that optimize isolated geometrical variables or assess collector performance without consideration of actual operational dynamics, this work undertook a simultaneous multi-parameter optimization of receiver height, mirror width and row spacing to maximize optical efficiency within a unified objective framework. The optimized solar field was subsequently embedded within a dynamic hourly hybrid system model incorporating thermal storage and fuelwood backup, enabling realistic assessment under continuous industrial operation. This coupling of geometric optimization with operational performance modeling provides a more comprehensive representation of real-world deployment conditions. An optimal solar multiple of 2.25 provided 14 hours of energy storage with average solar fractions ranging from 0.3853 to 0.5915 in low and high *DNI* months, respectively, highlighting the need for hybridization with fuelwood to ensure continuous energy supply. The hybrid configuration achieved a 48.84% reduction in annual tree consumption and associated CO_2 emissions, demonstrating meaningful environmental benefits while maintaining energy reliability. Beyond technical optimization, the study applied a multi-metric economic framework incorporating *SP*, *LCOH*, *NPV* and *IRR* to assess financial viability, with a sensitivity analysis covering performance uncertainties, capital and operating cost variability and macroeconomic fluctuations.

The optimal configuration achieved a payback period of 8.9 years, *NPV* of 1,288 USD, *IRR* of 12.78%, exceeding the prevailing interest rate. By undertaking simultaneous optimization of geometric parameters, dynamic hybrid system modeling and comprehensive economic assessment within a specific industrial application, this work advances LFR research toward holistic, deployable, and financially grounded solutions for industrial process heat. The framework is replicable and adaptable to other geographical and industrial contexts, thereby contributing practical value to the field.

ACKNOWLEDGEMENTS

Authors gratefully acknowledge the support provided by Kenyatta University through provision of study materials and guidance. The authors also acknowledge the support of the Kenya Tea Development Agency and Kenya Meteorological department for providing the study data.

NOMENCLATURE

Symbols

A_{fc}	filling coefficient	[-]
A_{p}	collector's aperture area	[m^2]
A_{T}	total ground area	[m^2]
$C_{\mathrm{c}}^{\mathrm{d}}$	direct costs	[USD/m^2]
C_{l}	land acquisition and preparation cost	[USD/m^2]
DC	direct costs	[USD]
DNI	direct normal irradiance	[W/m^2]
$E_{\mathrm{annual,thermal}}$	collected annual solar energy	[J]
f_{b}	blocking factor	[-]
f_{int}	intercept factor	[-]
f_{s}	shading factor	[-]
K_{a}	annuity factor	[%]
K_{e}	project efforts	[%]
K_{i}	insurance	[%]
$K_{\mathrm{O\&M}}$	operation and maintenance	[%]
K_{u}	uncertainties	[%]
$K\,(\Phi_{\mathrm{L}}, \Phi_{\mathrm{T}})$	longitudinal and transversal incidence angle modifiers	[-]
$LCOH$	levelized cost of heat	[USD]
$\dot{m}$	mass flow rate	[kg/s]
NPV	Net Present Value	[USD]
N_{ph}	number of photons	[-]
P_{abs}	power incident on absorber surface	[W]
P_{Ap}	power incident on collector surface	[W]
P_{ph}	power per photon	[W]
Q_{condabs}	conductive heat transfer between the inner and outer absorber tube surfaces	[W/m]
Q_{condgl}	conductive heat transfer between the inner and outer surfaces of the secondary reflector	[W/m]
Q_{condgl}	conductive heat transfer between the inner and outer glass cover surfaces	[W/m]
Q_{convenv}	convective heat transfer between outer glass surface and ambient air	[W/m]
Q_{convHTF}	convective heat transfer between the inner absorber tube surface and heat transfer fluid	[W/m]

$Q_{\text{convsrenv}}$	convective heat transfer between the outer secondary reflector surface and ambient air	[W/m]
Q_{solabs}	radiation absorbed by the absorber tube	[W/m]
Q_{solgl}	radiation absorbed by the glass cover	[W/m]
$Qu_{\_\text{total}}$	total useful heat gain	[W]
Q_{radann}	radiative heat transfer between the outer absorber tube and inner glass cover surfaces	[W/m]
Q_{radglsr}	radiative heat transfer between outer glass surface and the secondary reflector	[W/m]
Q_{radsenv}	radiative heat transfer between outer secondary reflector surface and environment	[W/m]
S	row spacing	[m]
$\hat{S}$	sun altitude angle	[°]
SOC	state of charge	[%]
T_{i}	fluid inlet temperature	[°C]
T_{o}	fluid outlet temperature	[°C]
V_{sa}	steam accumulator volume	[m^3]
W	primary mirror width	[m]

Greek letters

α_{s}	solar altitude angle	[°]
α_{T}	transverse solar altitude angle	[°]
β_{i}	angle between i^{th} mirror and horizontal ground plane	[°]
γ_{a}	annualized plant cost	[USD]
$\gamma_{\text{Total investment}}$	total investment	[USD]
η_{sa}	steam accumulator efficiency	[-]
η_{opt}	optical efficiency	[-]
η_{therm}	thermal efficiency	[-]
θ_{z}	zenith angle	[º]
ρ_{sl}	density of saturated liquid in	[kg m^{-3}]
Φ_{L}	longitudinal incidence angle	[°]
Φ_{T}	transversal incidence angle	[°]
ψ_{i}	mirror inclination angle	[°]
γ_{s}	solar azimuth angle	[°]

Abbreviations

CSP	Concentrated Solar Power
DSG	Direct Steam Generation
HTF	Heat Transfer Fluid
IAM	Incidence Angle Modifier
IRR	Internal Rate of Return
KMD	Kenya Meteorological Department
LFR	Linear Fresnel Reflector
MCRT	Monte Carlo Ray Tracing

MT	Made Tea
NSRD	National Solar Radiation Database
PMV	Pressure Maintaining Valve
PRV	Pressure Regulating Valve
PTC	Parabolic Trough Collector
SF	Solar Fraction
SM	Solar Multiple
TES	Thermal Energy Storage
VAT	Value Added Tax

REFERENCES

1. IEA, World Energy Outlook 2022, Paris, Oct. 2022, https://www.iea.org/reports/world-energy-outlook-2022, [Accessed: Nov. 17, 2024].
2. Intergovernmental Panel on Climate Change (IPCC), *Climate Change 2022 – Impacts, Adaptation and Vulnerability*. Cambridge University Press, 2023. https://doi.org/10.1017/9781009325844.
3. Z. Mirziyoyeva and R. Salahodjaev, Renewable energy and CO2 emissions intensity in the top carbon intense countries, *Renew. Energy*, Vol. 192, pp 507–512, 2022, https://doi.org/10.1016/j.renene.2022.04.137.
4. IEA, World Energy Outlook 2021, Paris, Oct. 2021, https://www.iea.org/reports/world-energy-outlook-2021, [Accessed: Nov. 17, 2024].
5. UNEP, Emissions Gap Report 2022: The Closing window - Climate crisis calls for rapid transformation of societies, Nairobi, 2022, https://www.unep.org/resources/emissions-gap-report-2022, [Accessed: Feb. 12, 2025].
6. S. H. Farjana, N. Huda, M. A. P. Mahmud, and R. Saidur, Solar process heat in industrial systems – A global review, *Renewable and Sustainable Energy Reviews*, Vol. 82, pp 2270–2286, Feb. 2018, https://doi.org/10.1016/j.rser.2017.08.065.
7. J. Sun, Z. Zhang, L. Wang, Z. Zhang, and J. Wei, Comprehensive Review of Line-Focus Concentrating Solar Thermal Technologies: Parabolic Trough Collector (PTC) vs Linear Fresnel Reflector (LFR), *Journal of Thermal Science*, Vol. 29, No. 5, pp 1097–1124, Oct. 2020, https://doi.org/10.1007/s11630-020-1365-4.
8. S. A. Kalogirou, Nontracking solar collection technologies for solar heating and cooling systems, *Advances in Solar Heating and Cooling*, 2016, pp 63–80, https://doi.org/10.1016/B978-0-08-100301-5.00004-7.
9. F. J. Sepúlveda, M. T. Miranda, I. Montero, J. I. Arranz, and F. J. Lozano, Analysis of Potential Use of Linear Fresnel Collector for Direct Steam Generation in Industries of the Southwest of Europe, *Energies (Basel).*, Vol. 12, No. 21, 4049, Oct. 2019, https://doi.org/10.3390/en12214049.
10. E. Bellos, C. Tzivanidis, and A. Papadopoulos, Optical and thermal analysis of a linear Fresnel reflector operating with thermal oil, molten salt and liquid sodium, *Appl. Therm. Eng.*, Vol. 133, pp 70–80, 2018, https://doi.org/10.1016/j.applthermaleng.2018.01.038.
11. A. Aljudaya, S. Michailos, D. B. Ingham, K. J. Hughes, L. Ma, and M. Pourkashanian, Techno-Economic Assessment of Molten Salt-Based Concentrated Solar Power: Case Study of Linear Fresnel Reflector with a Fossil Fuel Backup under Saudi Arabia's Climate Conditions, *Energies (Basel).*, Vol. 17, No. 11, 2719, 2024, https://doi.org/10.3390/en17112719.
12. D. Pulido-Iparraguirre, L. Valenzuela, J.-J. Serrano-Aguilera, and A. Fernández-García, Optimized design of a Linear Fresnel reflector for solar process heat applications, *Renew. Energy*, Vol. 131, pp 1089–1106, 2019, https://doi.org/10.1016/j.renene.2018.08.018.

13. M. Mokhtar, M. Berger, C. Zahler, H. Schenk, and R. Stieglitz, Direct Steam Generation for Process Heat using Fresnel Collectors, *Int. J. Therm. Environ. Eng.*, Vol. 10, No. 1, 2015, https://doi.org/10.5383/ijtee.10.01.001.
14. K. R. Kumar, K. Dashora, N. Krishnan, and S. Sanyal, Feasibility assessment of renewable energy resources for tea plantation and industry in India - A review, *Renewable and Sustainable Energy Reviews*, Vol. 145, 111083, 2021, https://doi.org/10.1016/j.rser.2021.111083.
15. B. P. Baruah, P. Khare, and P. G. Rao, The energy utilization pattern in tea industries of NE India and environmental issues, *Two and a Bud*, Vol. 59, pp 7–13, 2012.
16. C. W. Njiru and S. C. Letema, Energy Poverty and Its Implication on Standard of Living in Kirinyaga, Kenya, *Journal of Energy*, Vol. 2018, pp 1–12, Nov. 2018, https://doi.org/10.1155/2018/3196567.
17. J. J. Kibet and S. Letema, Energy use and greenhouse gas emissions in selected tea factories in Kenya, *PLOS Climate*, Vol. 3, No. 10, e0000329, Oct. 2024, https://doi.org/10.1371/journal.pclm.0000329.
18. ETP, KTDA Tea Factories: Thermal Manual, Ethical Tea Partnership, http://www.ethicalteapartnership.org/wp-content/uploads/2019/09/Thermal-Training-manual-new.pdf, [Accessed: Nov. 18, 2024].
19. J. D. Nixon and P. A. Davies, Cost-exergy optimisation of linear Fresnel reflectors, *Solar Energy*, Vol. 86, No. 1, pp 147–156, Jan. 2012, https://doi.org/10.1016/j.solener.2011.09.024.
20. J. Song, J. Ma, Z. Zhan, and Y. Dai, Optical Analysis and Optimization of the Linear Fresnel Collector's Mirror Field, in *Proceedings of the 2015 International Forum on Energy, Environment Science and Materials*, Paris, France: Atlantis Press, 2015, https://doi.org/10.2991/ifeesm-15.2015.90.
21. M. Babu, S. S. Raj, and A. Valan Arasu, Experimental analysis on Linear Fresnel reflector solar concentrating hot water system with varying width reflectors, *Case Studies in Thermal Engineering*, Vol. 14, 100444, 2019, https://doi.org/10.1016/j.csite.2019.100444.
22. A. Barbón, N. Barbón, L. Bayón, and J. A. Sánchez-Rodríguez, Optimization of the distribution of small-scale linear Fresnel reflectors on roofs of urban buildings, *Appl. Math. Model.*, Vol. 59, pp 233–250, 2018, https://doi.org/10.1016/j.apm.2018.01.040.
23. Y. Baba, H. Ajdad, A. Al Mers, A. Bouatem, B. Bououlid Idrissi, and S. El Alj, Preliminary cost-effectiveness assessment of a Linear Fresnel Concentrator: Case studies, *Case Studies in Thermal Engineering*, Vol. 22, 100730, 2020, https://doi.org/10.1016/j.csite.2020.100730.
24. M. A. Moghimi, K. J. Craig, and J. P. Meyer, Simulation-based optimisation of a linear Fresnel collector mirror field and receiver for optical, thermal and economic performance, *Solar Energy*, Vol. 153, pp 655–678, 2017, https://doi.org/10.1016/j.solener.2017.06.001.
25. P. O. O. Akello, C. O. Saoke, J. N. Kamau, and J. O. H. Ndeda, Assessment of measured and satellite-derived DNI databases for concentrated solar industrial thermal application in Kericho, Kenya, in *Proceedings of the 2022 Sustainable Research and Innovation Conference, JKUAT Main Campus, Kenya*, JKUAT, Oct. 2022.
26. R. Abbas, M. J. Montes, A. Rovira, and J. M. Martínez-Val, Parabolic trough collector or linear Fresnel collector? A comparison of optical features including thermal quality based on commercial solutions, *Solar Energy*, Vol. 124, pp 198–215, Feb. 2016, https://doi.org/10.1016/j.solener.2015.11.039.
27. E. González-Mora and M. D. Durán García, Methodology for an Opto-Geometric Optimization of a Linear Fresnel Reflector for Direct Steam Generation, *Energies (Basel).*, Vol. 13, No. 2, 355, Jan. 2020, https://doi.org/10.3390/en13020355.

28. M. J. Wagner, Results and Comparison from the SAM Linear Fresnel Technology Performance Model: Preprint, 2012, https://docs.nrel.gov/docs/fy12osti/54758.pdf, [Accessed: Aug. 08, 2025].
29. A. G. Olabi, Ed., *Renewable Energy - Volume 1: Solar, Wind and Hydropower: Definitions, Developments, Applications, Case Studies, and Modelling and Simulation*, Vol. 1. London: Academic Press, 2023.
30. S. Skouri, A. Ben Haj Ali, S. Bouadila, M. Ben Salah, and S. Ben Nasrallah, Design and construction of sun tracking systems for solar parabolic concentrator displacement, *Renewable and Sustainable Energy Reviews*, Vol. 60, pp 1419–1429, 2016, https://doi.org/10.1016/j.rser.2016.03.006.
31. E. Bellos and C. Tzivanidis, Development of analytical expressions for the incident angle modifiers of a linear Fresnel reflector, *Solar Energy*, Vol. 173, pp 769–779, Oct. 2018, https://doi.org/10.1016/j.solener.2018.08.019.
32. N. Kincaid, G. Mungas, N. Kramer, M. Wagner, and G. Zhu, An optical performance comparison of three concentrating solar power collector designs in linear Fresnel, parabolic trough, and central receiver, *Appl. Energy*, Vol. 231, pp 1109–1121, 2018, https://doi.org/10.1016/j.apenergy.2018.09.153.
33. E. Bellos, C. Tzivanidis, and M. A. Moghimi, Reducing the optical end losses of a linear Fresnel reflector using novel techniques, *Solar Energy*, Vol. 186, pp 247–256, 2019, https://doi.org/10.1016/j.solener.2019.05.020.
34. F. J. Pino, R. Caro, F. Rosa, and J. Guerra, Experimental validation of an optical and thermal model of a linear Fresnel collector system, *Appl. Therm. Eng.*, Vol. 50, No. 2, pp 1463–1471, 2013, https://doi.org/10.1016/j.applthermaleng.2011.12.020.
35. X. Duan, C. He, X. Lin, Y. Zhao, and J. Feng, Quasi-Monte Carlo ray tracing algorithm for radiative flux distribution simulation, *Solar Energy*, Vol. 211, pp 167–182, Nov. 2020, https://doi.org/10.1016/j.solener.2020.09.061.
36. H. Liang, S. You, and H. Zhang, Comparison of different heat transfer models for parabolic trough solar collectors, *Appl. Energy*, Vol. 148, pp 105–114, 2015, https://doi.org/10.1016/j.apenergy.2015.03.059.
37. B. Hafner, O. Stoppok, C. Zahler, M. Berger, K. Hennecke, and D. Krüger, Development of an Integrated Solar-fossil Powered Steam Generation System for Industrial Applications, *Energy Procedia*, Vol. 48, pp 1164–1172, 2014, https://doi.org/10.1016/j.egypro.2014.02.131.
38. R. N. Njuguna, F. Njoka, and J. Muguthu, Solar still basin measurements and liner material variance for improved water desalination efficiency, *Desalination Water Treat.*, Vol. 320, 100851, Oct. 2024, https://doi.org/10.1016/j.dwt.2024.100851.
39. M. Sengupta, Y. Xie, A. Lopez, A. Habte, G. Maclaurin, and J. Shelby, The National Solar Radiation Data Base (NSRDB), *Renewable and Sustainable Energy Reviews*, Vol. 89, pp 51–60, 2018, https://doi.org/10.1016/j.rser.2018.03.003.
40. W. Sun, Y. Hong, and Y. Wang, Operation Optimization of Steam Accumulators as Thermal Energy Storage and Buffer Units, *Energies (Basel).*, Vol. 10, No. 1, 17, 2016, https://doi.org/10.3390/en10010017.
41. F. Ordóñez, E. Flores, and R. Soria, Comprehensive analysis of the variables influencing the techno-economic optimization of medium temperature linear Fresnel collectors, *Energy Reports*, Vol. 7, pp 5747–5761, Nov. 2021, https://doi.org/10.1016/j.egyr.2021.08.194.
42. A. A. Imam, Y. A. Al-Turki, and R. S. Kumar, Techno-Economic Feasibility Assessment of Grid-Connected PV Systems for Residential Buildings in Saudi Arabi- A Case Study, *Sustainability*, Vol. 12, No. 1, 262, 2019, https://doi.org/10.3390/su12010262.
43. S. Khajepour and M. Ameri, Techno-economic analysis of using three Fresnel solar fields coupled to a thermal power plant for different cost of natural gas, *Renew. Energy*, Vol. 146, pp 2243–2254, Feb. 2020, https://doi.org/10.1016/j.renene.2019.08.075.

44. CBK, Inflation rates, Central Bank of Kenya, https://www.centralbank.go.ke/statistics/inflation-rates/, [Accessed: Dec. 31, 2024].
45. KRA, Import Duties, Kenya Revenue Authority, https://www.kra.go.ke/business/companies-partnerships/companies-partnerships-pin-taxes/company-partnership-imports-exemptions, [Accessed: Dec. 31, 2024].
46. KRA, Value-added-tax, Kenya Revenue Authority, https://www.kra.go.ke/individual/filing-paying/types-of-taxes/value-added-tax, [Accessed: Nov. 20, 2024].
47. CBK, Interest rates, Central Bank of Kenya, https://www.centralbank.go.ke/search/interest+rates/, [Accessed: Nov. 20, 2024].
48. KMD, State of the Climate Kenya 2023, Kenya Meteorological Department, https://meteo.go.ke/sites/default/files/downloads/SoC%20Kenya%202023_1.pdf, [Accessed: Nov. 26, 2024].
49. R. Soria, G. Caiza, N. Cartuche, J. López-Villada, and F. Ordoñez, Market potential of linear Fresnel collectors for solar heat industrial process in Latin-America-a case study in Ecuador, in *AIP Conference Proceedings*, AIP, 2020, 120003, https://doi.org/10.1063/5.0028503.
50. I. Purohit, P. Purohit, and S. Shekhar, Evaluating the potential of concentrating solar power generation in Northwestern India, *Energy Policy*, Vol. 62, pp 157–175, Nov. 2013, https://doi.org/10.1016/j.enpol.2013.06.069.
51. H. Ajdad, Y. Filali Baba, A. Al Mers, O. Merroun, A. Bouatem, and N. Boutammachte, Particle swarm optimization algorithm for optical-geometric optimization of linear fresnel solar concentrators, *Renew. Energy*, Vol. 130, pp 992–1001, Jan. 2019, https://doi.org/10.1016/j.renene.2018.07.001.
52. Z.-D. Cheng, X.-R. Zhao, Y.-L. He, and Y. Qiu, A novel optical optimization model for linear Fresnel reflector concentrators, *Renew. Energy*, Vol. 129, pp 486–499, Dec. 2018, https://doi.org/10.1016/j.renene.2018.06.019.
53. A. Roostaee and M. Ameri, Effect of Linear Fresnel Concentrators field key parameters on reflectors configuration, Trapezoidal Cavity Receiver dimension, and heat loss, *Renew. Energy*, Vol. 134, pp 1447–1464, Apr. 2019, https://doi.org/10.1016/j.renene.2018.09.053.
54. CBK, Key CBK Indicative Exchange Rates, https://www.centralbank.go.ke/forex/, [Accessed: Jan. 12, 2025].
55. R. Abbas and J. M. Martínez-Val, Analytic optical design of linear Fresnel collectors with variable widths and shifts of mirrors, *Renew. Energy*, Vol. 75, pp 81–92, 2015, https://doi.org/10.1016/j.renene.2014.09.029.
56. J. A. Duffie and W. A. Beckman, *Solar Engineering of Thermal Processes, Photovoltaics and Wind*. New Jersey: John Wiley & Sons, 2020.
57. A. Benidir, F. Khaldi, A. H. Benmachiche, and F. Bouras, Numerical thermal analysis of Shott 2008 PTR70 solar receiver under Hassi R'MEL power plant operation conditions, Journal of Engineering Science and Technology, Vol. 13, No. 1, pp 122–140, 2018.
58. T. L. Bergman and A. S. Lavine, *Fundamentals of Heat and Mass Transfer*, 8th ed. New Jersey: John Wiley & Sons, 2017.
59. O. N. Laban, C. M. Maghanga, and K. Joash, Determination of the Surface Roughness Parameter and Wind Shear Exponent of Kisii Region from the On-Site Measurement of Wind Profiles, *Journal of Energy*, Vol. 2019, pp 1–12, 2019, https://doi.org/10.1155/2019/8264061.
60. C. Saoke, J. N. Kamau, and R. Kinyua, Wind speed distribution, estimation of the wind shear exponent and the roughness parameter for Juja-Kenya, *Journal of Environmental Sciences and Resource Management*, Vol. 2, pp 121–137, Dec. 2010.

61. B. Shanmugapriya, K. S. Reddy, and T. Sundarajan, Performance investigation of linear evacuated absorber of 2-stage solar Linear Fresnel Reflector module under non-uniform flux distribution, *International Journal of Low-Carbon Technologies*, Vol. 13, No. 1, pp 92–101, 2018, https://doi.org/10.1093/ijlct/ctx024.
62. Y. Luo, X. Du, L. Yang, C. Xu, and M. Amjad, Impacts of solar multiple on the performance of direct steam generation solar power tower plant with integrated thermal storage, *Frontiers in Energy*, Vol. 11, No. 4, pp 461–471, 2017, https://doi.org/10.1007/s11708-017-0503-5.
63. M. Ploquin, S. Mer, A. Toutant, and F. Roget, CFD investigation of level fluctuations in steam accumulators as thermal storage: A direct steam generation application, *Solar Energy*, Vol. 245, pp 11–18, Oct. 2022, https://doi.org/10.1016/j.solener.2022.08.048.
64. C. Prieto, L. F. Cabeza, M. C. Pavón-Moreno, and E. Palomo, Thermal energy storage for direct steam generation concentrating solar power plants: Concept and materials selection, *J. Energy Storage*, Vol. 83, 110618, Apr. 2024, https://doi.org/10.1016/j.est.2024.110618.
65. A. Ehtiwesh, C. Kutlu, Y. Su, and S. Riffat, Modelling and performance evaluation of a direct steam generation solar power system coupled with steam accumulator to meet electricity demands for a hospital under typical climate conditions in Libya, *Renew. Energy*, Vol. 206, pp 795–807, Apr. 2023, https://doi.org/10.1016/j.renene.2023.02.075.

APPENDIX A1: Computation of intercept, blocking and shading loss factors

Figure 13 illustrates the shading between primary mirrors.

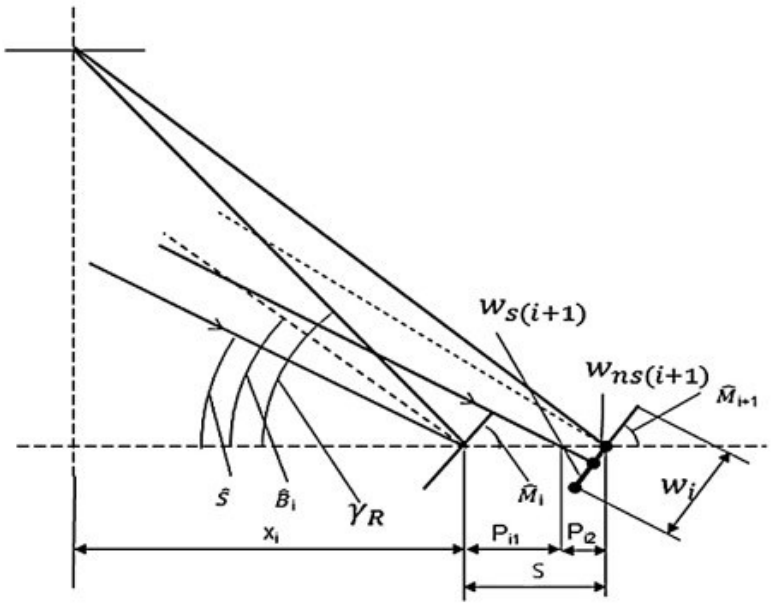

Figure 13. Shading between mirror rows in LFR field. Adopted from Abbas & Martinez [55]

The intercept factor is influenced by the mirror inclination and was determined using eq. (15):

$$f_{\text{int}} = \sum_{i=0}^{N} \left[\frac{h_{\text{fr}}}{2\left(\frac{W_{i+1}}{2} + S_{i+1}\right)} \right] \tag{15}$$

where N is the total number of rows, w denotes the primary mirror width and s denotes the row spacing.

The shading loss factor of mirrors i+1, $f_{s(i+1)}$, was computed using eq. (16) [55]:

$$f_{s(i+1)} = \frac{\frac{w_{i+1}}{2} - w_{ns(i+1)}}{w_{i+1}} \tag{16}$$

where the non-shaded fraction of the mirror width was calculated using eq. (17) [55]:

$$w_{ns(i+1)} = \min\left(\left(S - \frac{w_i}{2}\frac{\sin(\pi - \hat{S} - \acute{M}_i)}{\sin(\hat{S})}\right) \times \frac{\sin(\hat{S})}{\sin(\pi - \hat{S} - \acute{M}_{i+1})}, \frac{w_{i+1}}{2}\right) \tag{17}$$

For N number of rows, the total shading loss factor was determined using eq. (18):

$$f_s = \sum_{i=0}^{N}\left[\frac{\frac{w_{i+1}}{2} - w_{ns(i+1)}}{w_{i+1}}\right] \tag{18}$$

Eq. (15) to eq. (18) indicate that the shading factor depends on the spacing between mirror rows, S, sun altitude angle, $\hat{S}$, inclination angles of the mirrors in the various rows, $\acute{M}_{i+1}$, and mirror widths, w.

The blocking loss factor of mirror row i+1, $f_{b(i+1)}$, was calculated using eq. (19) [55]:

$$f_{b(i+1)} = \frac{\frac{w_{i+1}}{2} - w_{nb(i+1)}}{w_{i+1}} \tag{19}$$

where the width of the unobstructed portion of the half mirror was determined using eq. (20) [55]:

$$w_{nb(i+1)} = \min\left(\left(S - \frac{w_i}{2}\frac{\sin(\pi - \gamma_{Ri+1} - \acute{M}_i)}{\sin(\gamma_{Ri+1})}\right) \times \frac{\sin(\gamma_{Ri+1})}{\sin(\pi - \gamma_{Ri+1} - \acute{M}_{i+1})}, \frac{w_{i+1}}{2}\right) \tag{20}$$

For N number of rows, the total blocking loss factor was computed using eq. (21):

$$f_b = \sum_{i=0}^{N}\left[\frac{\frac{w_{i+1}}{2} - w_{nb(i+1)}}{w_{i+1}}\right] \tag{21}$$

The blocking factor depends on the spacing between mirror rows, the angle formed between transverse axis and the straight line connecting the mirror rotation axis to the receiver's centre line, γ_R, height of the receiver, inclination angles of the mirrors in the various rows, $\acute{M}$, $\acute{M}_{i+1}$, and mirror widths, w_i, w_{i+1}. γ_R was computed using eq. (22) and eq. (23) [55]:

$$\dot{B}_i = \frac{\gamma_R + \hat{S}}{2} \tag{22}$$

$$\acute{M}_i = \frac{\pi}{2} - \dot{B}_i \tag{23}$$

APPENDIX A2: Thermal model

Figure 14 illustrates the heat flow in the receiver.

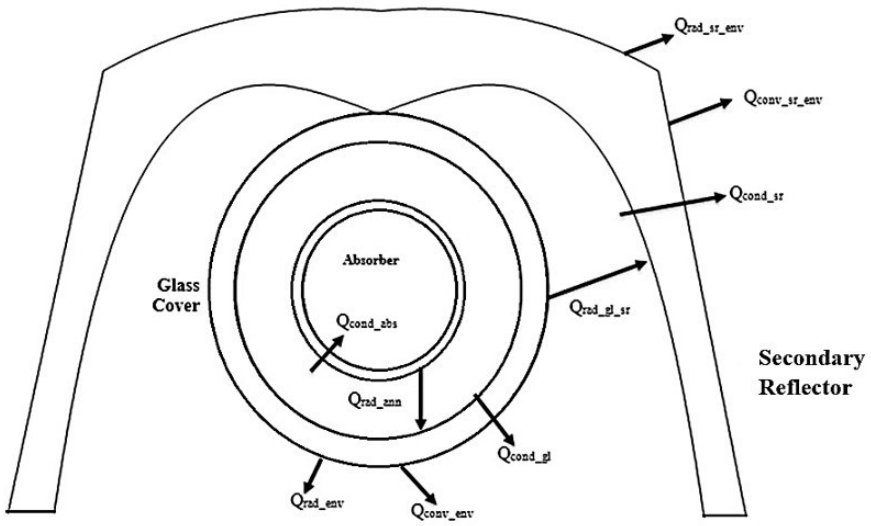

Figure 14. Heat flow in the evacuated tube receiver with secondary reflector

The heat transfer processes encompassing conduction, radiation and convection across different surfaces were quantified using the equations and correlations from reference models as detailed in **Table 10**.

Table 10. Heat transfer quantities

Quantity (W/m)	Reference model
Radiation absorbed by the absorber tube and glass cover (Q_{solabs}, Q_{solgl})	[56]
Convective heat transfer between the inner absorber tube surface and HTF, (Q_{convHTF})	[10], [56], [57]
Conductive heat transfer between the inner and outer absorber tube surfaces, (Q_{condabs})	[56]
Radiative heat transfer between the outer absorber tube and inner glass cover surfaces, (Q_{radann})	[56]
Conductive heat transfer between the inner and outer glass cover surfaces, (Q_{condgl})	[56]
Convective heat transfer between outer glass surface and ambient air, (Q_{convenv})	[56], [58], [59], [60]
Radiative heat transfer between outer glass surface and environment and the secondary reflector, (Q_{radenv}, Q_{radglsr})	[34]
Conductive heat transfer between the inner and outer surfaces of the secondary reflector, (Q_{condgl})	[56]
Convective heat transfer between the outer secondary reflector surface and ambient air, ($Q_{\text{convsrenv}}$)	[56], [61]
Radiative heat transfer between outer secondary reflector surface and environment (Q_{radenv})	[34]

To obtain the wind speed used in the computation of Reynold's number for convective heat transfer between the outer glass cover and ambient air and between outer surface of the secondary reflector and ambient air, the site wind speed was corrected based on the receiver height above the ground [60].

The energy balance at the various surfaces at steady state is expressed using eq. (24) to eq. (29):

$$Q_{\text{convsteam}} = Q_{\text{condabs}} \tag{24}$$

$$Q_{\text{solabs}} = Q_{\text{condabs}} + Q_{\text{radann}} \tag{25}$$

$$Q_{\text{condgl}} = Q_{\text{radann}} \tag{26}$$

$$Q_{\text{solgl}} + Q_{\text{condgl}} = Q_{\text{radsr}} + Q_{radenv} + Q_{convenv} \tag{27}$$

$$Q_{\text{condsr}} = Q_{\text{radsr}} \tag{28}$$

$$Q_{\text{condsr}} = Q_{\text{convsrenv}} + Q_{\text{radsrenv}} \tag{29}$$

The convective heat transfer on the inner surface of the secondary reflector was neglected in this model, as its influence on the useful heat gain by HTF is minimal.

APPENDIX A3: System Optimization and simulation

Geometric parameter optimization. An objective function was formulated for maximizing optical efficiency by optimizing the receiver height (H), mirror width (W) and row spacing (S). To achieve this, the intercept, shading loss and blocking loss factors were quantified iteratively. Eq. (3) to eq. (5), were combined as shown in eq. (30) where the number of photons reaching the receiver surface and optical efficiency were expressed as functions of H, W, and S:

$$\eta_{\text{opt}}(H,W,S) = \frac{N_{\text{ph}}(H,W,S) \times P_{\text{ph}}}{DNI \times A_{\text{p}}(W)} \tag{30}$$

From the intercept, shading loss and blocking loss factors computed in eq. (15), eq. (18) and eq. (21), respectively, the number of photons reaching the receiver was computed using eq. (31):

$$N_{\text{ph}}(H,W,S) = f_{\text{int}}(H,W,S) \times (1 - f_{\text{s}}(H,S,W)) \times (1 - f_{\text{b}}(H,W,S)) \times N_{\text{phi}}(W) \tag{31}$$

where f_{s} and f_{b} denotes the fraction of photons lost due to shading and blocking, respectively, and N_{phi} denotes the number of incident photons dependent on DNI and mirror area.

The total reflective aperture area was computed using eq. (32):

$$A_{\mathrm{P}} = L \times w \times N_{\mathrm{rows}} \tag{32}$$

where N_{rows} denotes the number of rows and L is a fixed length of the primary mirror.

Substituting eq. (31) and eq. (32) into eq. (30), the optical efficiency was computed using eq. (33), while the objective function was expressed by eq. (34):

$$\eta_{\mathrm{opt}}(H,W,S) = \frac{f_{\mathrm{int}}(H,W,S)\times\left(1-f_{\mathrm{s}}(H,W,S)\right)\times\left(1-f_{\mathrm{b}}(H,W,S)\right)\times N_{\mathrm{phi}}(W)\times P_{\mathrm{ph}}}{DNI\times L\times W\times N_{\mathrm{rows}}} \tag{33}$$

$$\text{Objective Function: } F(X) = \eta_{\mathrm{opt}}(X) \tag{34}$$

where X is the decision variable consisting of height of the receiver, H, mirror width, W and row spacing, S subject to the constraints and boundary conditions summarized in **Table 11**.

Table 11. Decision variables, boundary conditions and constraints

Number	Decision variables	Boundary Conditions	Constraints
1	H	[1, 15]	$0.5 \leq f_{\mathrm{int}} \leq 1$
2	W	[0.1, 2]	$0 \leq f_{\mathrm{b}} \leq 0.2$
3	S	[0.05, 1]	$0 \leq f_{\mathrm{s}} \leq 0.2$

Key constants in the optimization include the location's weighted average hourly direct normal irradiance (DNI), mirror length (L), power per photon (P_{ph}) and number of rows (N_{rows}).

Eq. (15) to eq. (23) are inherently multivariable and non-linear due to their angular dependencies and the inclusion of trigonometric functions. Consequently, the objective function was solved in MATLAB using the *fmincon* function, a nonlinear multivariable optimizer.

The other geometric parameters were kept constant as presented in **Table 12**.

Table 12. Fixed geometric parameters [57], [37]

Fixed parameters	
Number of rows	11
Number of mirrors	11
Length of each mirror	4 m
Length of absorber tube	4 m
Half acceptance angle of secondary reflector	46 °C

The optimization parameters were constrained to one decimal precision within the fmincon function to reflect realistic engineering tolerances and practical constructability considerations. To further examine the interdependence of geometric design variables, two-dimensional contour plots of optical efficiency were generated using the same objective function implemented in the *fmincon* optimization routine. The remaining variable was held at its optimized value.

System size optimization. The primary goal was to determine an appropriate LFR system size that maximizes the factory's fuelwood substitution while ensuring uninterrupted steam supply for tea processing, which operates in continuous 24-hour cycles. To achieve this, a thermal energy storage (TES) unit was employed in the direct steam generation (DSG) system. To enable storage, the analysis considered solar multiples (SM) greater than 1, allowing the system to generate excess steam beyond the instantaneous demand. SM is defined as the ratio of thermal energy supplied by a solar system to the actual thermal energy demand [62]. The average thermal energy demand during sunny hours was used to calculate SM values, and the corresponding storage capacities were evaluated based on average nighttime energy needs. The average daily thermal energy demand was computed using eq. (35):

$$D_{\text{thav}} = \frac{\sum_{n=1}^{12} \left[\frac{M_{\text{d}}}{N_{\text{da}}}\right]}{12} \tag{35}$$

where M_{d} denotes the monthly thermal energy demand and N_{da} represents the monthly factory operational days.

The average daily thermal energy demand during sunny hours was computed using eq. (36):

$$D_{\text{thsav}} = \frac{D_{\text{thav}} \times N_{\text{s}}}{24} \tag{36}$$

where N_{s} denotes the average daily sunny hours.

To achieve maximum substitution of fuelwood, a solar fraction (*SF*) of 1 was targeted. SF represents the ratio of the energy provided by the solar system to the total thermal energy demand. The *SF* values corresponding to the various system sizes were evaluated.

A Ruth's steam accumulator, a type of variable pressure storage and well suited for saturated steam applications, was selected for this study. Structurally, it consists of a vessel mostly filled with water and a small steam space above, enabling large latent heat storage [63]. These systems can be charged with steam at a relatively high pressure but are designed to discharge a lower pressure aligned with the process requirements [64]. In this study, the unit operated at a charging pressure of 12 bar and a discharging pressure of 8 bar, enhancing response capability while ensuring effective load matching.

The steam accumulator for the optimal system was sized using eq. (37) [40]:

$$V_{\text{sa}} = \frac{\dot{m} \times 3600 \times t_{\text{h}}}{\rho_{\text{sl}} \times \eta_{\text{sa}} \times A_{\text{fc}}} \tag{37}$$

where V_{sa} denotes the accumulator volume in m^3, $\dot{m}$ is the mass flow rate in kg/s, t_{h} is the storage time in hours, ρ_{sl} is the density of saturated liquid in kg/m^3, η_{sa} is the accumulator efficiency, typically 0.8 [65], and is the A_{fc} is the filling coefficient, typically 0.9 [40].

Paper submitted: 03.01.2026
Paper revised: 02.04.2026
Paper accepted: 11.04.2026